

Non-reciprocal Cavity Polariton with Atoms Strongly Coupled to Optical Cavity

Pengfei Yang,^{1,3,4,*} Ming Li,^{2,*} Xing Han,^{1,3} Hai He,^{1,3} Gang Li,^{1,3,†}
Chang-Ling Zou,^{2,1,‡} Pengfei Zhang,^{1,3} Yuhua Qian,^{4,5} and Tiancai Zhang^{1,3,§}

¹State Key Laboratory of Quantum Optics and Quantum Optics Devices,
and Institute of Opto-Electronics, Shanxi University, Taiyuan 030006, China

²CAS Key Laboratory of Quantum Information, University of Science and Technology of China, Hefei, Anhui 230026, P. R. China

³Collaborative Innovation Center of Extreme Optics, Shanxi University, Taiyuan 030006, China

⁴Institute of Big Data Science and Industry, Shanxi University, Taiyuan 030006, China

⁵Key Laboratory of Computational Intelligence and Chinese Information
Processing of Ministry of Education, Shanxi University, Taiyuan 030006, China

Breaking the time-reversal symmetry of light is of great importance for fundamental physics and has attracted increasing interest in the study of non-reciprocal photonic devices. Here, we experimentally demonstrate a chiral cavity QED system with multiple atoms strongly coupled to a Fabry-Pérot cavity. By polarizing the internal quantum state of the atoms, the time-reversal symmetry of the atom-cavity interaction is broken. The strongly coupled atom-cavity system can be described by non-reciprocal quasiparticles, i.e., the cavity polariton. When it works in the linear regime, the inherent nonreciprocity makes the system work as a single-photon-level optical isolator. Benefiting from the collective enhancement of multiple atoms, an isolation ratio exceeding 30 dB on the single-quanta level (~ 0.1 photon on average) is achieved. The validity of the non-reciprocal device under zero magnetic field and the reconfigurability of the isolation direction are also experimentally demonstrated. Moreover, when the cavity polariton works in the nonlinear regime, the quantum interference between polaritons with weak anharmonicity induces non-reciprocal nonclassical statistics of cavity transmission from coherent probe light.

I. INTRODUCTION

Magnet-free optical non-reciprocal devices, in which the light propagates non-reciprocally from opposite directions, have great application potential in photonic information processing [1, 2]. They also allow the realization of artificial gauge fields for photons and the simulation of interesting effects that were previously only available for electrons [3, 4]. The optical nonreciprocity (ONR) intrinsically relies on the time-reversal (T) symmetry breaking of photon propagation, which was traditionally realized via a notable magneto-optical effect with the precondition of an intense external bias DC-magnetic field [5]. However, the strong magnetic field and the associated nonreconfigurable and nonswitchable functionality greatly limits the applications [6]. Therefore, many efforts have been devoted to magnet-free ONR, including spatiotemporal modulation of dielectric permittivity [7–11], synthetic magnetic field [12–14], optics frequency conversion processes [15–22], optomechanics [23–28], chiral light-matter interaction [29–31], the Doppler effect [32–35] and light-induced magnetization [36] in atomic media, coherent interference of spin-waves [37], spinning resonators [38], etc. One of the most adopted approaches is to utilize coherent nonlinear optical effects, by which the direction-dependent transmission of the probe light is realized with a coherent external drive in a fixed direction [15–22] or a refractive index modulation with an effective momentum (p) [7–11]. The T-symmetry is broken as $\mathcal{T}p\mathcal{T}^{-1} = -p$ with \mathcal{T} being the time-reversal operator. All-optical nonreciprocity with such a mechanism has been experimentally verified in optomechanics and nonlinear microresonator platforms [17, 22, 23, 39], in which strong bias AC-driving fields are needed.

Alternatively, since $\mathcal{T}S\mathcal{T}^{-1} = -S$ for the spin operator S , the T-symmetry is naturally broken by preparing the internal spin state of atoms or emitters with $S \neq -S$. Therefore, when the photon interacts with atoms, assisted by the selection rules, the non-reciprocal transmission of the photon propagating along the z -direction could be realized by preparing the atoms to a ground state with biased spin state S_z . Recently, the strong coupling between single atoms or single quantum dots and chiral photons has been studied experimentally in a whispering-gallery-mode (WGM) microresonator [40] and nanowaveguide [41], where the non-reciprocal transmission of light fields can be realized via the unequal interaction strength between the emitters and photons with different chirality. The isolation [30] and circulation [42] of single photons have been demonstrated. In these experiments, the intrinsic chiral property of the evanescent field of the WGM microresonator or the nanowaveguide is adopted, but the achievable isolation ratio is limited to 13 dB due to the small atom number.

In this paper, the chiral light-matter interaction, where the interaction between atoms and two circular photons with orthogonal polarization are different, is introduced into the conventional cavity QED with an optical Fabry-Pérot cavity (FPC) experimentally. The collective interaction between multiple atoms with a miniature high-finesse optical FPC greatly boosts the cooperativity of the system, and the strongly coupled photons and atoms constitutes the hybrid quasiparticles, which are called “cavity polaritons”. The non-reciprocal polariton is then realized by preparing the atoms in a spin-polarized internal state with total spin $S \neq 0$, which asymmetrically couple to the two orthogonal circularly polarized cavity modes. The polariton inherently breaks the T-reversal symmetry and gives rise to non-reciprocal vacuum Rabi splitting

spectra. By introducing polarizers and waveplates outside the cavity, the circular polarization of inputs to the cavity is locked with the direction of the inputs, and thus, the non-reciprocal polaritons enable an optical isolator with an isolation over 30dB and a bandwidth exceeding 10MHz. Compared to our previous demonstration of ONR by using few-atom nonlinear bistability [43], which works on the few-photon level, this work is based on a vacuum-induced quantum process and works on the single-quanta level (~ 0.1 intracavity photon number on average). The isolation can be further enhanced by increasing the number of atoms. The direction of the isolation is reconfigurable by switching the internal state of spin-polarized atoms. The device is capable of working under a zero magnetic field with the aid of a circularly polarized optical pumping field propagating along the cavity to maintain the polarization of the atom.

Additionally, by employing the weak anharmonicity of the polaritons, nonclassical features of light can be generated non-reciprocally from coherent input light because of the quantum interference between polaritons. In particular, sub-Poissonian versus super-Poissonian photon statistics, or bunching versus antibunching effects, are observed when probing the system from different directions. Taking advantage of the few-atom cavity QED platform, the adjustable nonlinearity of non-reciprocal polaritons allows studies of potential non-reciprocal quantum effects and nonlinear dynamics. This new quasiparticle holds great potential for exploring quantum non-reciprocity in photonics [44, 45] and quantum network applications [46, 47], chiral photophysics of molecules [48] and new topological effects of polaritons [47, 49–52].

II. PRINCIPLE OF NON-RECIPROCAL CAVITY POLARITONS

Figure 1 schematically illustrates the concept of the chiral atom-cavity system. A cavity QED setup with neutral atoms coupled to an FPC [43, 53, 54] is adopted. The cavity supports two degenerate circularly polarized optical modes (σ_+ and σ_-), which asymmetrically couple to the atoms. Here, the σ_+ - and σ_- -polarized fields are defined by the rotating direction of the electric field with respect to the direction of the quantization axis (z -axis). It is worth noting that the σ_{\pm} polarization is not related to the propagation direction of the photon, and the σ_{\pm} -polarized field could be either a left-handed circularly polarized (LCP) field or a right-handed circularly polarized (RCP) field defined in optics, and the σ_+ -polarized and σ_- -polarized photons are chiral to each other (see Section S1 in the Supporting Information for details). In the following, we refer to the σ_{\pm} notation for describing the chiral photon-atom interaction since the corresponding atomic transitions with respect to the quantization axis couple with the σ_{\pm} -polarized photon according to the selection rules.

As shown in Figure 1 a and b, the σ_+ -polarized light field couples to the atomic transition $|g\rangle \leftrightarrow |e\rangle$, whereas no atomic transition is available for the σ_- -polarized light field. This sit-

uation can be easily found in an atom by preparing the atom to a ground spin-polarized state with Zeeman quantum number $m_F = -F$ (with the hyperfine quantum number $F \neq 0$) and using the atomic transition $|F\rangle \leftrightarrow |F'\rangle$ (with the hyperfine quantum number $F' \leq F$). The propagation direction of the signal light is not presented in Figure 1 because the interaction with the atom has no connection with the propagation direction. The collective atom-cavity coupling cooperativity for the σ_+ -polarized mode is much greater than unity, and cavity polaritons between the photons and atoms are then constituted. The cavity polaritons, shown as quasiparticles with annihilation operator $p_{u,l} = \frac{1}{\sqrt{2}}(a_+ \pm b_+)$ at the low excitation limit (u and l denote the upper and lower polaritons respectively; see Section S5 in the Supporting Information for details), have eigenfrequencies detuned from the bare cavity by $\pm g_{\text{eff}}$. Here, a_+ and b_+ denote the bosonic operator of the σ_+ -polarized cavity mode and the corresponding collective pseudospin operator for atomic transition, respectively, and g_{eff} is the effective coupling strength. Hence, the system shows two polariton states in the spectra (two peaks in Figure 1c), and both emit only σ_+ -polarized photons. When the time is reversed, the σ_+ -polarized photon becomes σ_- . The atoms are transparent to the σ_- -polarized photons due to the absence of atomic transitions (Figure 1b. Thus, the mode remains as a bare cavity mode (Figure 1d). Comparing these two cases, it is obvious that the T-symmetry is broken for the atom-cavity interacting system.

The T-symmetry breaking of the system would break the Lorentz reciprocity of forward ($+z$) and backward ($-z$) propagating probe light with σ_+ and σ_- polarizations, respectively. Under the linear approximation (Section S4 in the Supporting Information), the transmission of the whole system reads

$$T_{\pm} = \frac{4\kappa_1\kappa_2}{\kappa^2} \left| \frac{1}{i\Delta/\kappa + 1 + 2C_{\pm}/(i(\Delta + \Delta_{\text{ac}})/\gamma + 1)} \right|^2, \quad (1)$$

where \pm indicates the probe light condition ($+z, \sigma_+$) or ($-z, \sigma_-$). Here, κ and $\kappa_{1(2)}$ denote the total decay rate of the cavity mode and the external coupling rate to the cavity through mirror M1 (M2), respectively. Δ (Δ_{ac}) is the frequency detuning of the cavity modes to probe laser (atomic transition), and $C_{\pm} = g_{\text{eff},\pm}^2/(2\kappa\gamma)$ is the parameter of cooperativity for two σ -polarized cavity modes with $g_{\text{eff},\pm} = g_{\pm}\sqrt{N_{\text{eff}}}$, where N_{eff} is the effective intracavity atom number and g_{\pm} is the coupling strength of the σ_{\pm} cavity mode with one atom and depends on the atomic population distribution on the ground states. Beyond the linear approximation, the cavity polaritons actually exhibit anharmonicity for a finite atom number, with an effective Kerr coefficient $\mp g_{\text{eff}}/2N_{\text{eff}}$ for $p_{u,l}$ (Section S5 in the Supporting Information). In general, the atoms in thermal equilibrium would give a uniform population on ground state Zeeman levels, and the spin polarization would be absent with $S = 0$. Both σ_+ - and σ_- -polarized light couple to atoms with the same strengths with $C_+ = C_-$; therefore, the system is reciprocal. For a polarized spin state with a slanted population distribution on Zeeman

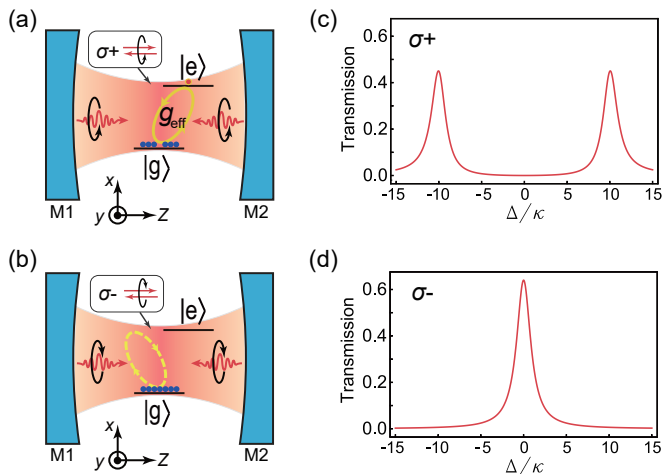


FIG. 1. Chiral interaction between atoms and a Fabry-Perot cavity. a) and b) are schematic illustrations of the chiral interaction, in which the σ_+ -mode of the cavity is strongly coupled to the atoms (a) but the σ_- -mode is transparent (b) due to the absence of the atomic transition. Here, the σ_+ -(σ_-) polarized field is defined by the rotating direction of the electric field with respect to the direction of the quantization axis (z -axis), which could be either an LCP field or an RCP field defined in optics (see Section S1 in the Supporting Information for details). In a) and b), $(+z)$ is taken as the quantization axis along the cavity. The propagation direction of the signal light is not presented because the interaction with the atom has no connection with the propagation direction. c) and d) are the theoretical predictions of the corresponding transmission spectra for the non-reciprocal interacting system by weak signals with polarizations of σ_+ (c) and σ_- (d), respectively. In c), two polariton states (the hybrid atom-photon states) are obviously observed. The parameters of $C_+ = 50$, $C_- = 0$, $\kappa = \gamma_+ = 1$, and $g_{\text{eff}}/\kappa = 10$ are used for the calculation.

levels (nonuniform distribution with $S \neq 0$), Eq. (1) predicts distinguishable spectra as $C_+ \neq C_-$, manifesting the nonreciprocity of the system.

III. RESULTS

A. Experimental setup

The experiments are performed on a cavity QED system with multiple cesium (Cs) atoms coupled to a miniature high-finesse FPC [43]. A sketch of the experimental system is shown in Figure 2a. A strongly coupled cavity QED system with multiple maximally spin-polarized Cs atoms is placed between the optical momentum-spin locking apparatuses, which consist of two sets of polarization beam splitters (PBSs) and quarter wave plates (QWPs), as shown in the dashed boxes of Figure 2a. The axis of the QWP is oriented 45° to the polarization of the transmitting light field from the PBS, and the optical axes of the two QWPs are orthogonal to each other. The probe light field with horizontally linear polarization transmits the apparatuses in both directions (from a1 to b2 and from a2 to b1), and the polarization is locked to

the propagating direction in the region between two QWPs, i.e., the probe light can only be in either $(+z, \sigma_+)$ or $(-z, \sigma_-)$ states with a fixed quantization axis (green arrow). Without special declarations, a weak 3-Gauss magnetic field is used to define the quantization axis. Without the cavity QED system or if a cavity QED system with atomic spin $S = 0$ is considered, the optical system is reciprocal. However, the reciprocity will be broken if a non-reciprocal cavity QED system (with atomic spin $S \neq 0$) is placed between the two QWPs. The whole system resembles a commercial isolator except that the Faraday rotator is replaced by a non-reciprocal cavity QED system. It is worth noting that, like the Faraday-rotator-based optical isolator, this device can also be used as a four-port circulator, and here, we only use it as an isolator by neglecting the reflections from the two PBSs.

The FPC is assembled by two concave mirrors with curvature radii of 100 mm, and the cavity length is $335 \mu\text{m}$. The concave surfaces are highly reflective, and the cavity has a finesse of 6.1×10^4 . A 1064 nm optical dipole trap (ODT) laser beam (horizontal) with a waist of $36 \mu\text{m}$ is used to load cold atoms from the MOT and transfer the atoms to the cavity. To prepare atoms to the maximally spin-polarized internal state, $S_z = -4$ ($|6S_{1/2}, F = 4, m_F = -4\rangle$), a σ_- -polarized 459 nm pump laser with a beam waist of $550 \mu\text{m}$ along the cavity axis and a linearly polarized 894 nm repump laser beam perpendicular to the cavity axis are used. The 459-nm and 894-nm lasers are resonant to Cs transitions $|6S_{1/2}, F = 4\rangle \leftrightarrow |7P_{1/2}, F' = 4\rangle$ and $|6S_{1/2}, F = 3\rangle \leftrightarrow |6P_{1/2}, F' = 4\rangle$, respectively. The coupling strength between the σ_+ -mode of the cavity and single atom is $g_+ = 2\pi \times 1.7$ MHz, and the decay rates of the cavity and the atom are $(\kappa, \gamma_+) = 2\pi \times (3.7, 2.6)$ MHz. When multiple atoms couple to the cavity, the collective coupling strength would surpass the decay rates of the cavity and atom and make the system work in the strong-coupling regime.

B. Demonstration of non-reciprocal polaritons

To demonstrate the non-reciprocal polariton, the bare cavity mode is tuned to be resonant to the atomic transition $|6S_{1/2}, F = 4, m_F = -4\rangle \leftrightarrow |6P_{3/2}, F' = 3, m_{F'} = -3\rangle$. We thus realize the ideal model shown in Figure 1a and b as only the σ_+ -mode couples to the atoms owing to the absence of an excited state for the σ_- -transition ($C_- = 0$) (the energy levels can be found in the inset of Figure 2a). The scattering matrix (\mathbf{S}_1) for the system is $\begin{pmatrix} 0 & 0 \\ \frac{4\kappa_1\kappa_2}{\kappa^2} & 0 \end{pmatrix}$ with $C_+ \gg 1$ and $\Delta = \Delta_{\text{ac}} = 0$ (see Section S4 in the Supporting Information for details).

By probing the system with σ_{\pm} -polarized light, we obtain the non-reciprocal vacuum Rabi splitting spectra, as shown in Figure 2b, which agree well with the theoretical predictions from Eq. (1) (Figure 1c and d). Vacuum Rabi splitting is observed only from the σ_+ -polarized probe, which indicates collective cooperativity $C_+ = 33.8(0.2)$ and an effective atom number $N_{\text{eff}} = 230.0(1.7)$. The atoms are optically

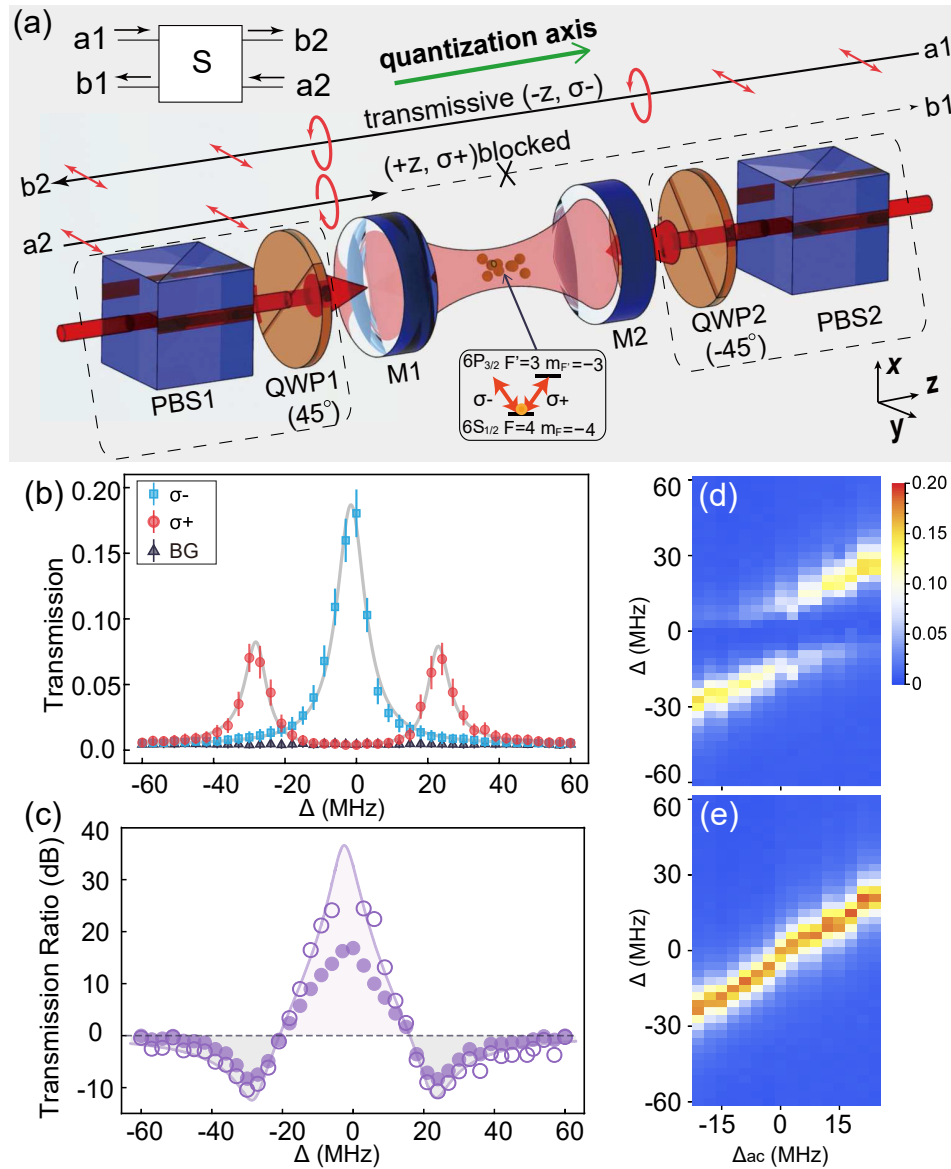


FIG. 2. Experimental demonstration of the chiral cavity QED system and non-reciprocal polaritons. a) A sketch of the experimental setup. A strongly coupled cavity QED system between multiple maximally spin-polarized Cs atoms and the σ_+ -polarized cavity mode is placed between two sets of PBSs and QWPs, where the locking of optical momentum-spin and the propagation direction can be realized. The quantization axis is along the cavity [green arrow, also the (+z) direction]. Red arrows indicate local optical polarization. A σ_+ polarized light propagating along the (+z) direction is blocked, while a σ_- polarized light propagating along the (-z) direction is transmitted. Insets: diagram of the atom energy levels (bottom) and scattering S matrix of the system (upper left corner). b) The measured transmission spectra with σ_+ (red circles) and σ_- (blue squares) polarized probes propagating along opposite directions. The background noise (black triangles) is shown as a comparison. The error bars correspond to one standard deviation of multiple measurements. The solid curves are the theoretical fittings by Eq. 1. c) The measured transmission ratio between the σ_{\mp} -polarized probe versus detuning. The parameters are the same as in b). The open and solid circles are the results with and without background correction, respectively, and the purple curve is the theoretical result. d) and e) Two-dimensional spectra of the system probed by σ_+ (d) and σ_- (e) polarized light with the probe-cavity detuning Δ scanned at different cavity-atom detunings Δ_{ac} .

pumped to the target spin state $|6S_{1/2}, F=4, m_F=-4\rangle$ with a fidelity of approximately 95%; thus, $C_- \ll C_+$ is still attained. The non-reciprocal polariton is further verified by the two-dimensional spectra (Figure 2d and e), where the characteristic avoid-crossing spectra for polaritons can be accessed with only σ_+ -polarized light as atom-cavity detuning Δ_{ac} be-

ing scanned.

In Figure 2b, if we focus on the frequency region around the atomic (or cavity) resonance, the transmission of the σ_+ -polarized probe is blocked, but the σ_- -polarized probe is transmitted. Since the two orthogonally polarized probe lights could only be injected into the cavity QED system from oppo-

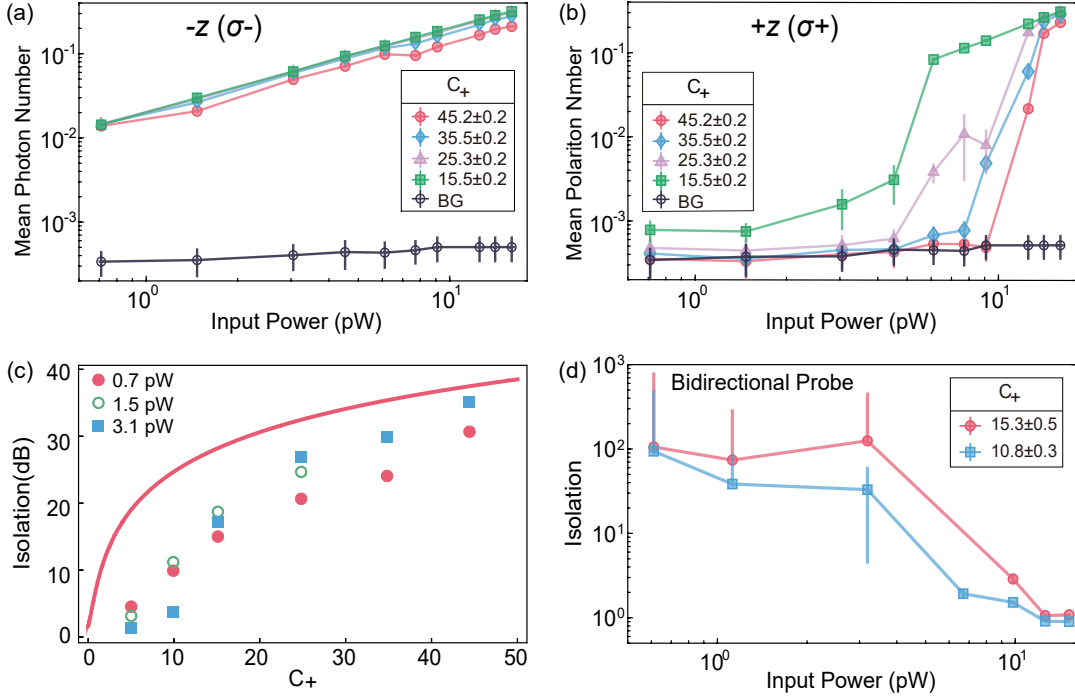


FIG. 3. Optical isolation based on the non-reciprocal cavity polaritons. a) and b) The measured intracavity mean photon number under a series of cooperativity C_+ versus input power of the probe propagating along the ($-z$) and ($+z$) directions, respectively. c) The measured isolation versus cooperativity C_+ under a series of input powers. The red solid circles, green open circles, and blue solid squares are for 0.7 pW, 1.5 pW, and 3.1 pW, respectively. d) The performance of the isolator with the forward and backward lights existing simultaneously, where the two lights have the same power. The corresponding cooperativities C_+ are 15.3(0.5) (red circles) and 10.8(0.3) (blue squares). The error bars correspond to one standard deviation.

site directions, the whole system actually operates as an optical isolator. The isolation is defined by the transmission ratio $\mathcal{I} = T_-/T_+$. Figure 2c presents the measured \mathcal{I} versus the probe detuning (Δ) with $\Delta_{ac} = 0$ and $C_+ = 33.8(0.2)$, showing both theoretical and experimental isolation over 20 dB with a bandwidth of 20 MHz. Around $\Delta \sim 0$, an isolation over 36.7 dB is expected from the theory, as the purple curve shows. However, the background-corrected experimental data points around $\Delta = 0$ are absent because the residual transmission of the blocked field is much weaker than the background, which makes the background-corrected value inaccessible from the fluctuation of the background with the current data integration time of 100 μ s. We believe the actual isolation around $\Delta = 0$ should be comparable with the theoretical prediction. We can also see that an isolation of approximately -10 dB can also be obtained when the probe is resonant to the polariton states.

The large \mathcal{I} around zero detuning confirms the high performance of the optical isolator based on the non-reciprocal polariton in our scheme. From Eq. (1), when $\Delta_{ac} = \Delta = 0$, the ideal isolation

$$\mathcal{I}_{\max} = (1 + 2C_+)^2 \quad (2)$$

would be achieved. \mathcal{I}_{\max} increases quadratically with the cooperativity C_+ , and over 30-dB isolation can be achieved as $C_+ \geq 15.3$.

We then comprehensively investigate the performance of the isolator by varying the intracavity atom number (N_{eff}) and probe intensity under the condition $\Delta_{ac} = \Delta = 0$, and the results are summarized in Figure 3. The ($-z, \sigma_-$) light couples to an empty cavity mode (Figure 1d), and the transmission depends linearly on the input light power (Figure 3a). The slight decrease in the transmission at larger C_+ is because of the scattering of the atom with imperfections in state preparations. An overall transmission of 18% is obtained and is limited by the impedance mismatch of the FPC [43]. A much higher transmission would be achieved by optimizing impedance matching of the cavity. For a given C_+ , in Figure 3b, the transmission of the ($+z, \sigma_+$) light is blocked at weak input power with a corresponding mean photon number less than 0.1, as expected. However, the input field can also excite the polariton modes off-resonantly, which would degrade the isolation ratio as the input power increases with a fixed atom number. The polariton modes will be fully saturated at a certain input power which depends on the atom number. The larger C_+ (also the larger atom number) is, the more difficult it is for the polariton modes to be excited and the better the isolation obtained. The dependence of the measured isolation \mathcal{I} on C_+ compared with the theoretical curve (Eq. 2) is shown in Figure 3c. Although the measured \mathcal{I} is slightly lower than the theoretical value \mathcal{I}_{\max} (red solid curve), which is mainly limited by the experimental imper-

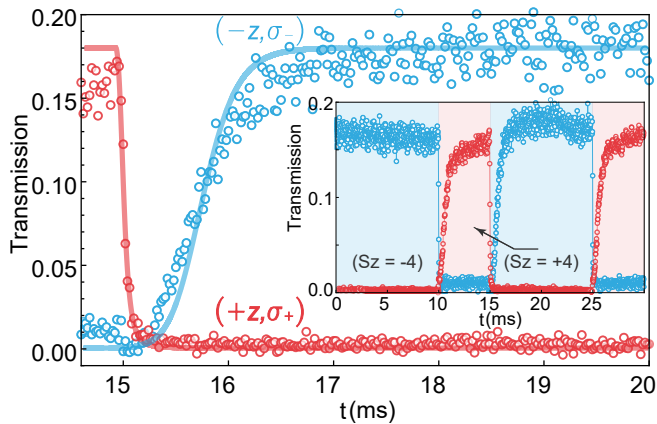


FIG. 4. Reconfiguration of the isolation direction. Measured transmission as a function of time accompanied by atomic state switching between $S_z = -4$ and $+4$, where $C_{+(-)} = 20.5$. The blue open circles (experiment) and solid line (theory) are for forward light ($-z, \sigma_-$), and the red ones are for backward light ($+z, \sigma_+$). The switching times are 705 ± 19 and $43 \pm 2 \mu\text{s}$ for the shut-off and turn-on processes, respectively. The inset shows the switching of the isolator continuously. The experimental data points are the average of 230 trials with 0.01 mean probe photons inside the FPC.

fections, such as background noise and the finite fidelity of the target spin-polarized atomic state preparation as discussed above, the measured isolation can still reach 30 dB with C_+ of approximately 35.

C. Performance of the optical isolator with two opposite laser beams coexisting

Different from many other magnet-free optical nonlinear non-reciprocal devices, the optical isolator demonstrated in this article can work in the condition with coexisting forward and backward light due to the decoupling of the two circularly polarized cavity modes. This property would dramatically expand the application. The isolation is experimentally verified with the input power varying in this bidirectional-probing scenario, and the data for $C_+ = 15.3(0.5)$ and $10.8(0.3)$ are shown by red circles and blue squares in Figure 3d, respectively. The behavior is quite similar to that of single-direction probing, where a higher C_+ gives higher isolation with weak input power. However, because both the forward and backward lights are shined, it is very difficult to separate the transmission of the backward light from the residual reflection of the forward light, and the measured isolation is slightly lower. The actual isolation should be the same as the case with an individual probing light field.

D. Reconfigurability of the optical isolator

Moreover, our device is reconfigurable by controlling the internal state of spin-polarized atoms. This is done experi-

mentally by manipulating the population of the atomic Zeeman states. To verify this, the circularity of the 459-nm laser is switched between σ_- and σ_+ polarization with a time period of 15 ms to switch the atomic population between states $S_z = -4$ ($|6S_{1/2}, F = 4, m_F = -4\rangle$) and $S_z = 4$ ($|6S_{1/2}, F = 4, m_F = +4\rangle$) back and forth. The blocking and transmitting directions are then reconfigured accordingly (Figure 4). Here, a constant 1.5-Gauss magnetic field is applied to maintain the spin polarization of atoms. We find that the shut-off time $43 \pm 2 \mu\text{s}$ is much faster than the turn-on time $705 \pm 19 \mu\text{s}$. The difference between these two switching times is due to the different joint effects of optical pumping and atom-cavity coupling in the two processes. The detailed analysis can be found in the Supporting Information (Section S11). The theoretical curves of the switching calculated by taking both the optical pumping process and the atom-cavity couplings in all Zeeman states into account are also shown in Figure 4 (solid curves). The experimental results (open circles) are in good agreement with the theoretical prediction.

E. Validity of the isolation without a magnetic field

The non-reciprocal cavity polariton and the demonstration of the aforementioned optical isolator are performed with a weak bias magnetic field. Notably, even such a weak magnetic field is not necessary for our current device. The performance of the isolation under a zero magnetic field is demonstrated and measured when the atoms are continuously pumped with a σ_- -polarized 459 nm optical pumping laser, by which the spin direction of atoms can be preserved. The data are shown in Figure 5. Here, the atomic polarization is degraded due to the absence of the quantization axis previously defined by the magnetic field. However, the presence of the σ_- -polarized 459 nm pump laser can weakly maintain the polarization, and thus, the system still gives non-reciprocal spectra, as shown in Figure 5a, where blue (red) open circles are for the σ_- (σ_+) polarized probe. The corresponding isolation of the probe light fields is shown in Figure 5b, which gives an isolation around 4dB with a bandwidth over 30 MHz. It should be noted that by increasing the power of the polarized 459 nm optical pumping laser, a better isolation performance can be achieved.

F. Non-reciprocal quantum statistics

The non-reciprocal polariton is then studied in more general cases since the maximally polarized spin state might not always be available in experiments. For example, as schematically illustrated in Figure 6a, both the σ_+ - and σ_- -modes of the cavity could strongly couple to the atomic transition with unequal strengths ($C_{\pm} \gg 0$ and $C_- \neq C_+$). The situation is realized by preparing the atom to state $|6S_{1/2}, F = 4\rangle$ with a slanted population on the Zeeman sublevels from $m_F = -4$ to $m_F = 4$ (yellow solid circles). The cavity is then tuned to be

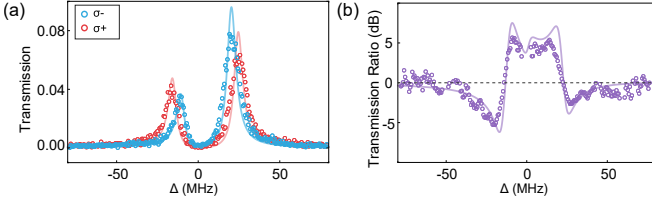


FIG. 5. Validity of the isolation without a magnetic field. a) The non-reciprocal spectra for the σ_+ (open red circles) and σ_- (open blue circles) probes. The solid curves are the theoretical fittings by Eq. 1. b) The transmission ratio with zero magnetic field, where a 4-dB isolation with bandwidth of 30 MHz is maintained. The purple solid curve is the theoretical expectation from the two fitting curves in a).

resonant to $|6S_{1/2}, F=4\rangle \leftrightarrow |6P_{3/2}, F'=5\rangle$. Owing to the unequal transition strength (arrows with different thicknesses in Figure 6a), not only is the frequency of the polaritons asymmetric, but the strength of the nonlinearity experienced by the polariton is also different. The spectra of the polariton probed by weak coherent light, shown in Figure 6b, verify the non-reciprocity of the polariton. Here, the system is probed with σ_+ - and σ_- -polarized light both in the ($+z$) direction, which is equivalent to the case in which the system is probed by the ($+z, \sigma_+$)- and ($-z, \sigma_-$)-probing configurations. The spectra of two σ_+ -polaritons are asymmetric due to the off-resonant coupling between the bare cavity modes and other hyperfine energy levels ($|6P_{3/2}, F'=4\rangle$) of the atoms, which induces a 6-MHz frequency shift in the effective cavity mode. In particular, such a dispersive effect is also non-reciprocal and is similar to the avoid-crossing results for large atom-cavity detuning in Figure 2d.

In such a few-atom cavity QED system, the anharmonicity of the polariton is inversely proportional to $\sqrt{N_{\text{eff}}}$ (Section S5 in the Supporting Information). The quantum effects of the polariton are greatly suppressed because the Kerr coefficient is much smaller than the system dissipation rate ($g_{\text{eff}}/2N_{\text{eff}} \ll \kappa, \gamma$). Surprisingly, we theoretically predict that the transmitted light exhibits remarkable quantum statistics for a classical input, as shown by the second-order correlation $g^{(2)}(0)$ in Figure 6b (blue and red dashed lines). When the probe is near resonant to the polariton states, the emissions of both σ_{\pm} -polaritons show a slight deviation from the Poissonian statistic ($g^{(2)}(0) = 1$) due to the weak anharmonicity of the polaritons. In contrast, much more pronounced nonreciprocity of the quantum statistics occurs around $\Delta = 0$, where the super-Poissonian distribution ($g^{(2)}_{\sigma_+}(0) > 1$) versus the sub-Poissonian distribution ($g^{(2)}_{\sigma_-}(0) < 1$) is expected (indicated by the vertical black-dotted line with mark “c” in Figure 6b). The physical mechanism behind the extraordinary behavior with $\Delta \sim 0$ is the quantum interference between the two polariton states p_{\pm} , which possesses a Kerr coefficient with opposite signs (Section S5 in the Supporting Information).

The experimental results of the temporal second-order correlation functions $g^{(2)}(\tau)$ for the σ_{\pm} -modes at $\Delta = 0$ are shown

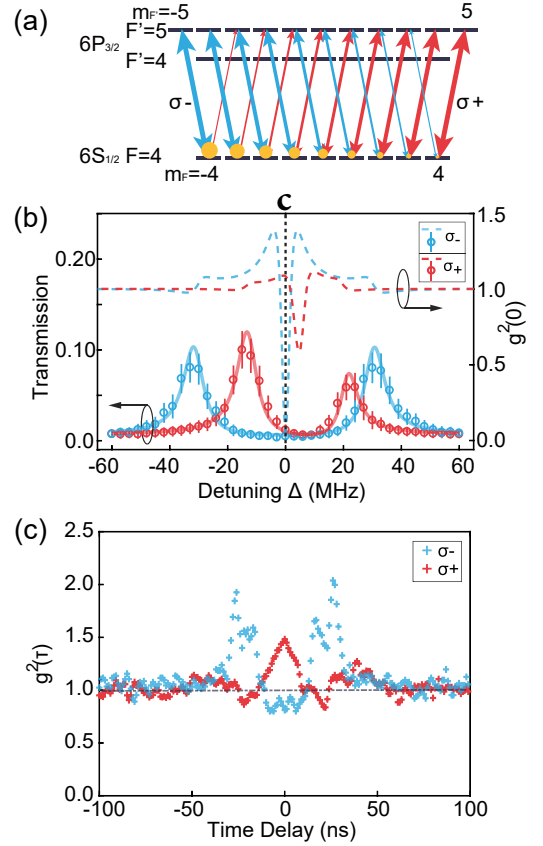


FIG. 6. Quantum interference of polaritons and the nonreciprocity of quantum statistics. a) The energy diagram for realizing non-reciprocal polaritons under more general conditions. The atom ground spin state has a slanted population distribution on m_F . The size of yellow solid circles indicates the population in every Zeeman sublevel. The thickness of the blue (σ_-) and red (σ_+) arrows represents the corresponding σ -transition strength. b) The measured spectra by probing the system with σ_+ (red open circles) and σ_- (blue open circles) polarization. The fitting of the data gives $C_+ = 15.1(0.3)$, $C_- = 50.8(0.6)$, and $\Delta_{\text{ac}} = 0$ for the σ_- mode and $\Delta_{\text{ac}} = 6$ MHz for the σ_+ mode. The theoretical expectations of the second-order correlation function $g^{(2)}(0)$ are displayed as dashed curves, and the nonreciprocity of quantum statistics is clearly presented. c) The measured temporal second-order correlation function $g^{(2)}(\tau)$ by detecting the emitted photons from the cavity with the probe-cavity detuning fixed at 0 MHz. The error bars correspond to one standard deviation.

in Figure 6c, where the red (blue) cross markers are for the σ_+ - (σ_-) mode. Here, we investigate the nonclassical statistics of the emission from cavity polaritons excited by a forwarding probe beam with fixed power. For the σ_+ -polariton, the probe frequency is actually closer to one polariton state and shows a super-Poissonian distribution ($g^{(2)}(0) \sim 1.5$) and bunching effect ($g^{(2)}(0) > g^{(2)}(\tau)$). In contrast, the probe is equally off-resonant to both σ_- -polaritons, where significant destructive interference of cavity polaritons takes place. The sub-Poissonian distribution ($g^{(2)}(0) \sim 0.8$) and anti-bunching effect ($g^{(2)}(0) < g^{(2)}(\tau)$) are displayed (Section S6 in the Supporting Information). The deviation between the experi-

mental and theoretical results may be attributed to the noise background and system parameter uncertainties. Additionally, there are substantial oscillations in the temporal correlation function for both σ_{\pm} -polaritons, which indicate quantum interference between different polariton states. These results suggest that the anharmonicity of polaritons would bring non-reciprocal quantum features, which would extend the concept of non-reciprocal devices to the quantum regime [45] and provide experimental insights into the unconventional bosonic blockade effect [55].

IV. CONCLUSION

Our demonstration of non-reciprocal polaritons from both linear and nonlinear aspects opens up a new perspective for research on cavity QED as well as novel non-reciprocal devices for photonics. The collective effect of a small atom ensemble produces polariton states as a hybridization of light and matter. By manipulating the atom at a maximally polarized state, the polariton can only be accessed optically from a certain direction, allowing isolation of photons with an isolation ratio exceeding 30dB on the single-photon level. The reconfigurability of the isolation directions is experimentally demonstrated by switching the polarization of the atoms. The validity of the isolator with zero magnetic field is verified with relatively low isolation. By manipulating the quantum interference between the polaritons, the weak anharmonicity could still generate non-reciprocal nonclassical outputs from classical input. With the direction-dependent bunching and anti-bunching properties of polaritons being observed for the first time, our experiments show the potential for realizing both linear and nonlinear non-reciprocal optics effects on the single-quanta level. Such quantum non-reciprocal polariton states can be extended to phonons [56] and microwave photons [57, 58] by harnessing their coupling with electron spin ensembles, and could find applications as quantum routers and isolators for quantum networks [47]. Our work also initiates the exploration of the concept of quantum nonreciprocity with conventional quantum optics systems from two perspectives: on the one hand, polaritons are inherently a hybrid quantum state of photons and atoms, so superpositions of reciprocal and non-reciprocal polariton states are worth further investigation. On the other hand, we can study the quantum behaviors of non-reciprocal polaritons utilizing their intrinsic anharmonicity.

Supporting Information

Supporting Information is available from the author.

Acknowledgements

We thank H J. Kimble for helpful discussions. We also thank Ya-Nan Lv for her help in the numerical simulations. This work was supported by the National Key Research and Development Program of China (Grant Nos. 2021YFA1402002 and 2017YFA0304502), the National Natural Science Foundation of China (Grant No. U21A6006, U21A20433, 11974223,

11974225, 12104277, and 12104278), and the Fund for Shanxi 1331 Project Key Subjects Construction. M.L. and C.-L.Z. were supported by National Natural Science Foundation of China (Grant No.11674342 and 11922411), and the Program of State Key Laboratory of Quantum Optics and Quantum Optics Devices.

Conflict of interest

The authors declare no competing interests.

Data Availability Statement

The data that support the findings of this study are available from the corresponding author upon reasonable request.

* These authors contributed equally to this work.

† gangli@sxu.edu.cn

‡ clzou321@ustc.edu.cn

§ tczhang@sxu.edu.cn

- [1] D. Jalas, A. Petrov, M. Eich, W. Freude, S. Fan, Z. Yu, R. Baets, M. Popović, A. Melloni, J. D. Joannopoulos, M. Vanwolleghem, C. R. Doerr, and H. Renner, “What is – and what is not – an optical isolator,” *Nat. Photonics* **7**, 579 (2013).
- [2] V. S. Asadchy, M. S. Mirmoosa, A. D’Áaz-Rubio, S. Fan, and S. A. Tretyakov, “Tutorial on electromagnetic nonreciprocity and its origins,” *Proceedings of the IEEE* **108**, 1684 (2020).
- [3] N. Goldman, G. Juzeliunas, P. Öhberg, and I. B. Spielman, “Light-induced gauge fields for ultracold atoms,” *Rep. Prog. Phys.* **77**, 126401 (2014).
- [4] D. Hey and E. Li, “Advances in synthetic gauge fields for light through dynamic modulation,” *R. Soc. Open Sci.* **5**, 172447 (2018).
- [5] R. J. Potton, “Reciprocity in optics,” *Rep. Prog. Phys.* **67**, 717 (2004).
- [6] L. Bi, J. Hu, P. Jiang, D. H. Kim, G. F. Dionne, L. C. Kimerling, and C. a. Ross, “On-chip optical isolation in monolithically integrated non-reciprocal optical resonators,” *Nat. Photonics* **5**, 758 (2011).
- [7] Z. Yu and S. Fan, “Complete optical isolation created by indirect interband photonic transitions,” *Nat. Photonics* **3**, 91 (2009).
- [8] D.-W. Wang, H.-T. Zhou, M.-J. Guo, J.-X. Zhang, J. Evers, and S.-Y. Zhu, “Optical diode made from a moving photonic crystal,” *Phys. Rev. Lett.* **110**, 093901 (2013).
- [9] S. A. R. Horsley, J.-H. Wu, M. Artoni, and G. C. La Rocca, “Optical nonreciprocity of cold atom bragg mirrors in motion,” *Phys. Rev. Lett.* **110**, 223602 (2013).
- [10] D. L. Sounas and A. Alù, “Non-reciprocal photonics based on time modulation,” *Nat. Photonics* **11**, 774 (2017).
- [11] H. Ramezani, P. K. Jha, Y. Wang, and X. Zhang, “Nonreciprocal localization of photons,” *Phys. Rev. Lett.* **120**, 043901 (2018).
- [12] L. Tzuang, K. Fang, P. Nussenzveig, S. Fan, and M. Lipson, “Non-reciprocal phase shift induced by an effective magnetic flux for light,” *Nat. Photonics* **8**, 701 (2014).
- [13] L. Yuan, S. Xu, and S. Fan, “Achieving nonreciprocal unidirectional single-photon quantum transport using the photonic aharonov–bohm effect,” *Opt. Lett.* **40**, 5140 (2015).
- [14] K. Fang, J. Luo, A. Metelmann, M. H. Matheny, F. Marquardt, A. A. Clerk, and O. Painter, “Generalized non-reciprocity in an

- optomechanical circuit via synthetic magnetism and reservoir engineering,” *Nat. Phys.* **13**, 465 (2017).
- [15] A. Kamal, J. Clarke, and M. Devoret, “Noiseless nonreciprocity in a parametric active device,” *Nat. Phys.* **7**, 311 (2010).
- [16] N. A. Estep, D. Sounas, J. Soric, and A. Alù, “Magnetic-free non-reciprocity and isolation based on parametrically modulated coupled-resonator loops,” *Nat. Phys.* **10**, 923 (2014).
- [17] S. Hua, J. Wen, X. Jiang, Q. Hua, L. Jiang, and M. Xiao, “Demonstration of a chip-based optical isolator with parametric amplification,” *Nat. Commun.* **7**, 13657 (2016).
- [18] F. Song, Z. Wang, E. Li, Z. Huang, B. Yu, and B. Shi, “Optical nonreciprocity using four-wave mixing in hot atoms,” *Appl. Phys. Lett.* **119**, 024101 (2021).
- [19] C. Li, Q. Yu, Y. Zhang, M. Xiao, and Z. Zhang, “Optical isolation with optical parametric amplification in an atomic system,” *Laser & Photonics Reviews* **17**, 2200267 (2023).
- [20] L. Chang, X. Jiang, S. Hua, C. Yang, J. Wen, L. Jiang, G. Li, G. Wang, and M. Xiao, “Parity-time symmetry and variable optical isolation in active-passive-coupled microresonators,” *Nat. Photonics* **8**, 524 (2014).
- [21] K. Xia, F. Nori, and M. Xiao, “Cavity-free optical isolators and circulators using a chiral cross-kerr nonlinearity,” *Phys. Rev. Lett.* **121**, 203602 (2018).
- [22] X. Guo, C.-L. Zou, H. Jung, and H. X. Tang, “On-chip strong coupling and efficient frequency conversion between telecom and visible optical modes,” *Phys. Rev. Lett.* **117**, 123902 (2016).
- [23] Z. Shen, Y.-L. Zhang, Y. Chen, C.-L. Zou, Y.-F. Xiao, X.-B. Zou, F.-W. Sun, G.-C. Guo, and C.-H. Dong, “Experimental realization of optomechanically induced non-reciprocity,” *Nat. Photonics* **10**, 657 (2016).
- [24] F. Ruesink, M.-A. Miri, A. Alù, and E. Verhagen, “Nonreciprocity and magnetic-free isolation based on optomechanical interactions,” *Nat. Commun.* **7**, 13662 (2016).
- [25] E. Verhagen and A. Alù, “Optomechanical nonreciprocity,” *Nat. Phys.* **13**, 922 (2017).
- [26] J. Kim, M. Kuzyk, K. Han, H. Wang, and G. Bahl, “Non-reciprocal Brillouin scattering induced transparency,” *Nat. Phys.* **11**, 275 (2015).
- [27] M. Kang, A. Butsch, and P. Russell, “Reconfigurable light-driven opto-acoustic isolators in photonic crystal fibre,” *Nat. Photonics* **5**, 549 (2011).
- [28] E. A. Kittlaus, W. M. Jones, P. T. Rakich, N. T. Otterstrom, R. E. Muller, and M. Rais-Zadeh, “Electrically driven acousto-optics and broadband non-reciprocity in silicon photonics,” *Nat. Photonics* **15**, 43 (2021).
- [29] I. Shomroni, S. Rosenblum, Y. Lovsky, O. Bechler, G. Guendelman, and B. Dayan, “All-optical routing of single photons by a one-atom switch controlled by a single photon,” *Science* **345**, 903 (2014).
- [30] I. Söllner, S. Mahmoodian, S. Lindskov Hansen, L. Midolo, A. Javadi, G. Kirsanske, T. Pregnolato, H. El-Ella, E. Hye Lee, J. Dong Song, S. Stobbe, and P. Lodahl, “Deterministic photon-emitter coupling in chiral photonic circuits,” *Nat. Nanotechnol.* **10**, 775 (2015).
- [31] O. Bechler, A. Borne, S. Rosenblum, G. Guendelman, O. Ezrahi Mor, M. Netser, T. Ohana, Z. Aqua, N. Drucker, R. Finkelstein, Y. Lovsky, R. Bruch, D. Gurovich, E. Shafir, and B. Dayan, “A passive photon-atom qubit swap operation,” *Nat. Phys.* **14**, 996 (2018).
- [32] S. Zhang, Y. Hu, G. Lin, Y. Niu, K. Xia, J. Gong, and S. Gong, “Thermal-motion-induced non-reciprocal quantum optical system,” *Nat. Photonics* **12**, 744 (2018).
- [33] G. Lin, S. Zhang, Y. Hu, Y. Niu, J. Gong, and S. Gong, “Non-reciprocal amplification with four-level hot atoms,” *Phys. Rev. Lett.* **123**, 033902 (2019).
- [34] C. Liang, B. Liu, A.-N. Xu, X. Wen, C. Lu, K. Xia, M. K. Tey, Y.-C. Liu, and L. You, “Collision-induced broadband optical nonreciprocity,” *Phys. Rev. Lett.* **125**, 123901 (2020).
- [35] M.-X. Dong, K.-Y. Xia, W.-H. Zhang, Y.-C. Yu, Y.-H. Ye, E.-Z. Li, L. Zeng, D.-S. Ding, B.-S. Shi, G.-C. Guo, and F. Nori, “All-optical reversible single-photon isolation at room temperature,” *Sci. Adv.* **7**, eabe8924 (2021).
- [36] X.-X. Hu, Z.-B. Wang, P. Zhang, G.-J. Chen, Y.-L. Zhang, G. Li, X.-B. Zou, T. Zhang, H. X. Tang, C.-H. Dong, G.-C. Guo, and C.-L. Zou, “Noiseless photonic non-reciprocity via optically-induced magnetization,” *Nat. Commun.* **12**, 2389 (2021).
- [37] X. Lu, W. Cao, W. Yi, H. Shen, and Y. Xiao, “Nonreciprocity and quantum correlations of light transport in hot atoms via reservoir engineering,” *Phys. Rev. Lett.* **126**, 223603 (2021).
- [38] S. Maayani, R. Dahan, Y. Kligerman, E. Moses, A. U. Hassan, H. Jing, F. Nori, D. N. Christodoulides, and T. Carmon, “Flying couplers above spinning resonators generate irreversible refraction,” *Nature* **558**, 569 (2018).
- [39] D. B. Sohn, S. Kim, and G. Bahl, “Time-reversal symmetry breaking with acoustic pumping of nanophotonic circuits,” *Nat. Photonics* **12**, 91 (2018).
- [40] C. Junge, D. O’Shea, J. Volz, and A. Rauschenbeutel, “Strong coupling between single atoms and nontransversal photons,” *Phys. Rev. Lett.* **110**, 213604 (2013).
- [41] C. Sayrin, C. Junge, R. Mitsch, B. Albrecht, D. O’Shea, P. Schneeweiss, J. Volz, and A. Rauschenbeutel, “Nanophotonic optical isolator controlled by the internal state of cold atoms,” *Phys. Rev. X* **5**, 041036 (2015).
- [42] M. Scheucher, A. Hilico, E. Will, J. Volz, and A. Rauschenbeutel, “Quantum optical circulator controlled by a single chirally coupled atom,” *Science* **354**, 1577 (2016).
- [43] P. Yang, X. Xia, H. He, S. Li, X. Han, P. Zhang, G. Li, P. Zhang, J. Xu, Y. Yang, and T. Zhang, “Realization of nonlinear optical nonreciprocity on a few-photon level based on atoms strongly coupled to an asymmetric cavity,” *Phys. Rev. Lett.* **123**, 233604 (2019).
- [44] K. Xia, G. Lu, G. Lin, Y. Cheng, Y. Niu, S. Gong, and J. Twamley, “Reversible nonmagnetic single-photon isolation using unbalanced quantum coupling,” *Phys. Rev. A* **90**, 043802 (2014).
- [45] R. Huang, A. Miranowicz, J.-Q. Liao, F. Nori, and H. Jing, “Nonreciprocal photon blockade,” *Phys. Rev. Lett.* **121**, 153601 (2018).
- [46] J. Borregaard, A. S. Sørensen, and P. Lodahl, “Quantum Networks with Deterministic Spin-Photon Interfaces,” *Adv. Quantum Technol.* **2**, 1800091 (2019).
- [47] P. Lodahl, S. Mahmoodian, S. Stobbe, P. Schneeweiss, J. Volz, A. Rauschenbeutel, H. Pichler, and P. Zoller, “Chiral quantum optics,” *Nature* **541**, 473 (2017).
- [48] S. Sun, B. Gu, and S. Mukamel, “Polariton ring currents and circular dichroism of mg-porphyrin in a chiral cavity,” *Chem. Sci.* **13**, 1037 (2022).
- [49] A. A. Houck, H. E. Türeci, and J. Koch, “On-chip quantum simulation with superconducting circuits,” *Nat. Phys.* **8**, 292 (2012).
- [50] D. G. Angelakis, ed., *Quantum Simulations with Photons and Polaritons*, Quantum Science and Technology (Springer International Publishing, Cham, 2017).
- [51] H. Zhao, X. Qiao, T. Wu, B. Midya, S. Longhi, and L. Feng, “Non-hermitian topological light steering,” *Science* **365**, 1163 (2019).

- [52] T. P. Lyons, D. J. Gillard, C. Leblanc, J. Puebla, D. D. Solnyshkov, L. Klompmaker, I. A. Akimov, C. Louca, P. Muduli, A. Genco, M. Bayer, Y. Otani, G. Malpuech, and A. I. Tartakovskii, “Giant effective zeeman splitting in a monolayer semiconductor realized by spin-selective strong light-matter coupling,” *Nature Photonics* **16**, 632 (2022).
- [53] J. M. Raimond, M. Brune, and S. Haroche, “Colloquium: Manipulating quantum entanglement with atoms and photons in a cavity,” *Rev. Mod. Phys.* **73**, 565 (2001).
- [54] A. Reiserer and G. Rempe, “Cavity-based quantum networks with single atoms and optical photons,” *Rev. Mod. Phys.* **87**, 1379 (2015).
- [55] H. J. Snijders, J. A. Frey, J. Norman, H. Flayac, V. Savona, A. C. Gossard, J. E. Bowers, M. P. Van Exter, D. Bouwmeester, and W. Löffler, “Observation of the Unconventional Photon Blockade,” *Phys. Rev. Lett.* **121**, 43601 (2018).
- [56] D. A. Golter, T. Oo, M. Amezcuca, K. A. Stewart, and H. Wang, “Optomechanical Quantum Control of a Nitrogen-Vacancy Center in Diamond,” *Phys. Rev. Lett.* **116**, 143602 (2016).
- [57] S. Putz, D. O. Krimer, R. Amsüss, A. Valookaran, T. Nöbauer, J. Schmiedmayer, S. Rotter, and J. Majer, “Protecting a spin ensemble against decoherence in the strong-coupling regime of cavity QED,” *Nat. Phys.* **10**, 720 (2014).
- [58] A. Bienfait, J. J. Pla, Y. Kubo, X. Zhou, M. Stern, C. C. Lo, C. D. Weis, T. Schenkel, D. Vion, D. Esteve, J. J. L. Morton, and P. Bertet, “Controlling spin relaxation with a cavity,” *Nature* **531**, 74 (2016).
- [59] D. A. Steck, “Cesium d line data,” *Cesium D Line Data (revision 2.2.1, <http://steck.us/alkalidata>)* (2019).
- [60] H. Flayac and V. Savona, “Unconventional photon blockade,” *Phys. Rev. A* **96**, 053810 (2017).
- [61] J. Johansson, P. Nation, and F. Nori, “Qutip 2: A python framework for the dynamics of open quantum systems,” *Computer Physics Communications* **184**, 1234 (2013).

V. SUPPLEMENTARY INFORMATION FOR: NON-RECIPROCAL CAVITY POLARITON WITH ATOMS STRONGLY COUPLED TO OPTICAL CAVITY

Pengfei Yang^{1,3,4,†}, Ming Li^{2,†}, Xing Han^{1,3}, Hai He^{1,3}, Gang Li^{1,3,*}, Chang-Ling Zou^{2,1,*}, Pengfei Zhang^{1,3}, Yuhua Qian^{4,5} and Tiancai Zhang^{1,3,*}

¹State Key Laboratory of Quantum Optics and Quantum Optics Devices, and Institute of Opto-Electronics, Shanxi University, Taiyuan 030006, China.

²CAS Key Laboratory of Quantum Information, University of Science and Technology of China, Hefei 230026, China.

³Collaborative Innovation Center of Extreme Optics, Shanxi University, Taiyuan 030006, China.

⁴Institute of Big Data Science and Industry, Shanxi University, Taiyuan 030006, China.

⁵Key Laboratory of Computational Intelligence and Chinese Information Processing of Ministry of Education, Shanxi University, Taiyuan 030006, China.

Corresponding author E-mail:

Gang Li, gangli@sxu.edu.cn

Chang-Ling Zou, clzou321@ustc.edu.cn

Tiancai Zhang, tczhang@sxu.edu.cn

The supplementary material presents a theoretical analysis of non-reciprocal cavity polaritons and single-photon-level optical isolation, simulation of the reconfiguration of the isolator, experimental setups and time sequences.

S1. Circularly polarized light in atomic physics and optics

For circularly polarized light, the electric-field vector rotates around the wave propagation direction. The definitions of circular polarization are different in atomic physics and optics. The relations of the circularly polarized light fields with definitions in atomic physics and optics are summarized in Figure S1(a).

In optics, the polarization is defined by the rotation direction of the electric field by looking against the propagation direction of the light beam. The polarization is defined as left-handed circular polarization (LCP) for a counterclockwise rotation of the electric field. The right-handed circular polarization (RCP) is for a clockwise rotation of the electric field.

In atomic physics, however, the polarization of light is defined by the rotation direction of the electric field regardless of the propagating direction but with respect to a quantization direction. The direction is often provided by a magnetic field. In this scenario, σ_- (σ_+) polarized light is light with its electric field rotating clockwise (counterclockwise) if viewed against the quantized direction. When interacting with an atomic dipole, the σ_- (σ_+) polarized light drives atomic transition with a change in the Zeeman quantum number $\Delta m_F = -1$ ($+1$). We also find that the two circularly polarized photons defined in atomic physics are chiral photons. The depictions of the chiral photons are displayed in Figure S1(b), in which the σ_- -polarized and σ_+ -polarized photons are well described by the left and right hands, respectively.

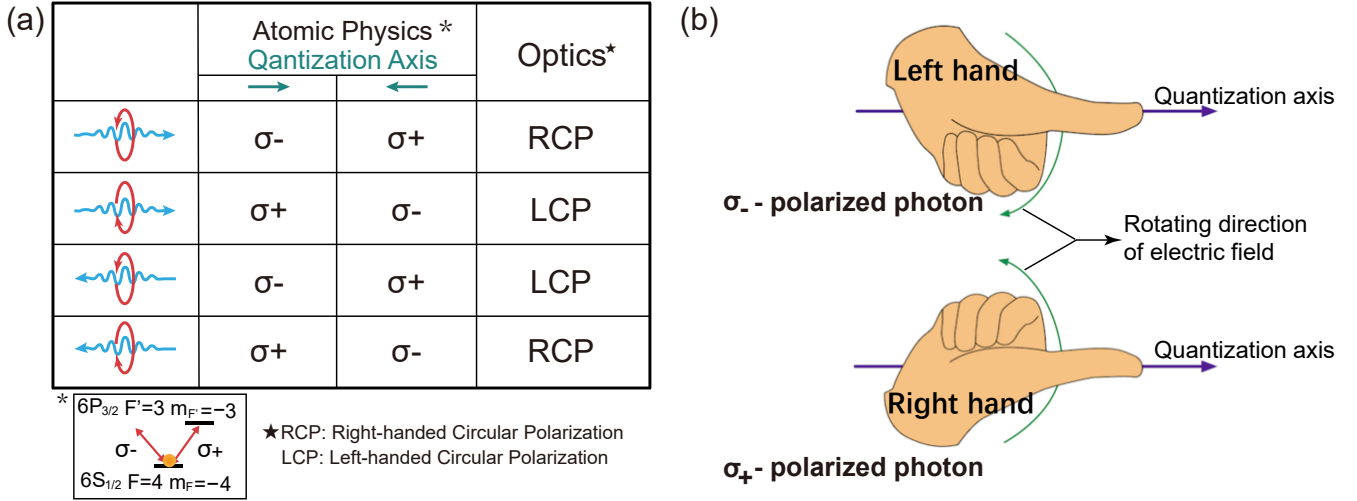


FIG. S1. Circularly polarized light. (a) Descriptions of circularly polarized light in atomic physics and optics. The first row displays the rotation of the electric field and the propagation directions for a light field. The second row is the classification of the polarization in atomic physics, where a quantization axis is referenced. The third row gives the classification of the polarization in optics. The small inset shows the energy levels and corresponding σ transitions we used to demonstrate the non-reciprocal cavity polaritons and the single-photon-level isolator in the maintext. (b) Depictions of the chiral photons where σ_- -polarized and σ_+ -polarized photons are described by the left and right hands, respectively.

In our experiment demonstrating the chiral interaction and the optical isolator, σ_+ -polarized light drives the transition from $|6S_{1/2}, F=4, m_F=-4\rangle$ to $|6P_{3/2}, F'=3, m_F=-3\rangle$, and σ_- -polarized light does not interact with the atom due to the absence of the corresponding Zeeman sublevel $m_F=-5$ in the excited state $|6P_{3/2}, F'=3\rangle$. The energy level diagram and the corresponding interactions are shown in the inset of Figure S1(a).

In the experiment demonstrating the non-reciprocal quantum statistics, state $|6P_{3/2}, F'=5\rangle$ is adopted as the excited state. In this case, the σ_- (σ_+) polarized light drives atomic transition with the change in Zeeman quantum number $\Delta m_F = -1$ ($+1$) between states $|6S_{1/2}, F=4\rangle$ and $|6P_{3/2}, F'=5\rangle$. The transition strengths are different for the Zeeman state with $m_F = -4$ to $+4$ in state $|6S_{1/2}, F=4\rangle$, which can be found in the Cesium D Line Data [59].

S2. Experimental setups and time sequences

As shown in Figure S2, the experimental setup consists of a horizontally oriented high-finesse Fabry-Pérot cavity with a length of $335\ \mu\text{m}$, and the TEM_{00} mode has a waist of $33.3\ \mu\text{m}$. A $1064\ \text{nm}$ optical dipole trap (ODT) laser beam (horizontal) with a waist of $36\ \mu\text{m}$ is used to load cold atoms from the MOT and transfer the atoms to the cavity. The beam direction is perpendicular

to the cavity axis. The output of the cavity is the emission of the cavity polaritons or bare cavity modes, is recorded by single photon counting modules (SPCMs). The parameters of the cavity quantum electrodynamics (QED) system are $(g_0, \kappa, \gamma) = 2\pi \times (1.7, 3.7, 2.6)$ MHz, where g_0 is the maximal single atom-cavity coupling strength for the σ_+ transition of ^{133}Cs $|6S_{1/2}, F=4, m_F=-4\rangle \leftrightarrow |6P_{3/2}, F'=3, m_{F'}=-3\rangle$, κ is the cavity field decay rate, and γ is the atomic excitation decay rate. An auxiliary 840 nm laser beam along the cavity axis is used to stabilize and control the length of the cavity. A 459 nm laser with a waist of $550 \mu\text{m}$ oriented along the cavity axis and a 894 nm repump laser beam perpendicular to the cavity axis are used to prepare the atom in the Zeeman state $|6S_{1/2}, F=4, m_F=-4\rangle$.

Figure S3a shows the variance of the parameter of cooperativity C_+ versus time during the experiment when the atoms flow from the MOT to the cavity mode. C_+ is deduced from the vacuum Rabi splitting, as shown in the inset of the figure. The time sequences for the experiment are shown in Figure S3b. Cold atoms are initially accumulated in a mirror-reflected magneto-optical trap (MOT) from the background atomic vapor, and the atom cloud is approximately 8 mm away from the cavity center. An additional 5 ms polarization gradient cooling procedure is performed to precool the atoms, and the repumping laser of the MOT is kept at 2 ms to pump atoms into state $|6S_{1/2}, F=4\rangle$. The ODT and optical pumping lasers are switched on before shutting off the MOT lasers. Since the ODT is aligned to overlap with the MOT and the waist is set at the right middle of the MOT and the cavity, cold atoms can be guided and successively transported into the cavity by the ODT after shutting off the MOT. The MOT is kept from 0-2010 ms for atom loading, during which an ODT is applied at 1900 ms and is kept for 460 ms until the atomic assemble flows out of the cavity mode. The 459 nm and 894 nm laser beams are kept on throughout the measurement to prepare atoms in state $|6S_{1/2}, F=4, m_F=-4\rangle$ continuously. The single photon counting module (SPCM) records the transmitted photon of the cavity from 2025 ms to 2450 ms to characterize the non-reciprocal polaritons in the few-atom cavity QED system.

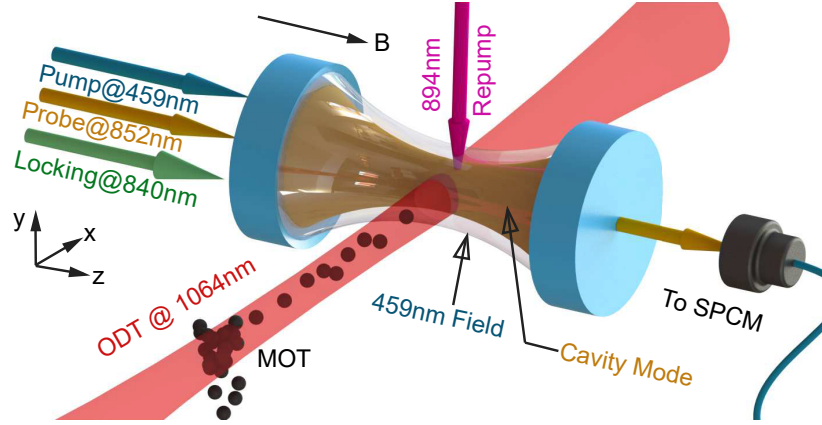


FIG. S2. Experimental apparatus. A high-finesse Fabry-Pérot cavity is horizontally oriented, and an MOT is located ~ 8 mm beside the cavity mode (horizontal). The laser beam of the ODT at 1064 nm is utilized to transport atoms from the MOT into the cavity mode. A weak probe beam along the axis of the cavity and SPCMs are implemented to record the transmission of the cavity.

S3. Model

For our experimental setup, the atoms pass through the cavity field with a duration of ~ 1 ms, which is orders longer than the relaxation times of the atom and cavity; thus, we treat the system as steady state at any instance. The Hamiltonian that describes the coupling between a single-mode field and N two-level atoms is

$$H = \Delta a^\dagger a + \frac{\Delta'}{2} \sum_{i=1}^N s_z^i + \sum_{i=1}^N g_i (a^\dagger s_-^i + a s_+^i) \quad (\text{S1})$$

where a (a^\dagger) is the annihilation (creation) operator of the cavity field, $\Delta' = \Delta + \Delta_{ac}$, Δ is the probe-cavity detuning, Δ_{ac} is the atom-cavity detuning, s_-^i and s_+^i represent the lowering and raising operators of the transition of the i -th atom and fulfill $[s_+^i, s_-^i] = s_z^i$, and g_i is the atom-cavity strength for the i -th atom. Here, the full model is very difficult to solve in practice when $N > 15$, due to the high computational complexity. By approximately treating the coupling between a few atom ensemble and the cavity as an N -atom ensemble uniformly coupled with the cavity, i.e., $g_i = g$, the collective behavior of the N atoms can be

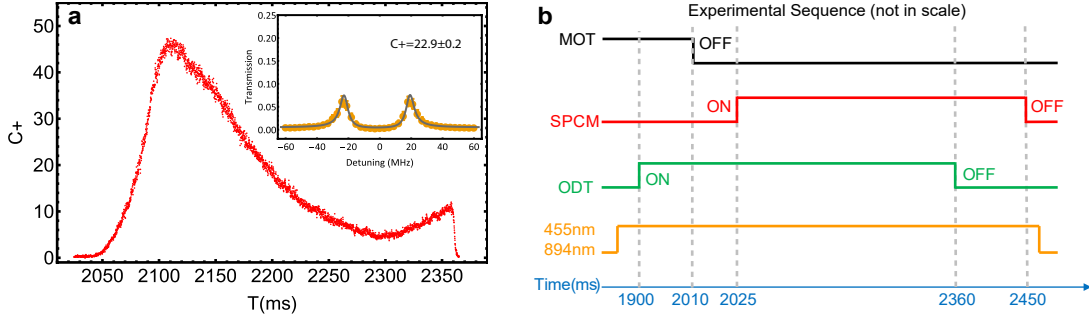


FIG. S3. Determination of C_{\pm} and experimental sequences. (a) The collective atom-cavity coupling cooperativity C_+ during measurements. The red dots indicate the C_+ for each moment during the experiment, and they are extracted from atom transportation 600 times. C_+ is extracted from the transmission spectra by fitting the vacuum Rabi splitting spectrum, as shown in the inset figure, where $C_+ = 22.9 \pm 0.2$. C_- is determined by the similar method. In our experiments, the cold atoms move very slowly (\sim cm/s). As a result, although the atom number inside the cavity varies with time, the measurement of the system with duration on the ms-level reflects the instantaneous state of the system. (b) shows the detailed time sequence of the experiment. The MOT is open from 0 to 2010 ms for atom loading. The ODT is applied at 1900 ms and is kept for 460 ms until the atomic assemble transit through the cavity mode. The 455 nm and 894 nm laser beams are kept on throughout the measurement to ensure that the atoms are always in state $|6S_{1/2}, F = 4, m_F = -4\rangle$. The SPCM records the transmission of the cavity from 2025 ms to 2450 ms.

treated as a $N/2$ spin with operators

$$L_+ = \sum_{i=1}^N s_+^i \quad (S2)$$

$$L_- = \sum_{i=1}^N s_-^i \quad (S3)$$

$$L_z = \sum_{i=1}^N s_z^i \quad (S4)$$

It is easy to verify that $[L_+, L_-] = \sum_i^N [s_+^i, s_-^i] = L_z$. The spin operator can be transformed to a bosonic operator by the Holstein-Primakoff transformation,

$$L_+ = \sqrt{N} b^\dagger \sqrt{1 - \frac{b^\dagger b}{N}} \quad (S5)$$

$$L_- = \sqrt{N} \sqrt{1 - \frac{b^\dagger b}{N}} b \quad (S6)$$

$$L_z = [L_+, L_-] = -N + 2b^\dagger b \quad (S7)$$

Neglecting the constant term $-N$, the Hamiltonian is transformed to

$$\begin{aligned} H &= \Delta a^\dagger a + \Delta' b^\dagger b + g (a^\dagger L_- + a L_+) \\ &= \Delta a^\dagger a + \Delta' b^\dagger b + g \sqrt{N} \left[\sqrt{1 - \frac{b^\dagger b}{N}} a^\dagger b + a b^\dagger \sqrt{1 - \frac{b^\dagger b}{N}} \right], \end{aligned} \quad (S8)$$

which describes the interaction between two bosonic modes. The square root of the bosonic operator can be expanded in Taylor series as

$$\sqrt{1 - \frac{b^\dagger b}{N}} = 1 - \frac{b^\dagger b}{2N} - \frac{(b^\dagger b)^2}{8N^2} - \dots \quad (S9)$$

In the following analysis, we assume that the system is probed with a low excitation level, i.e., the excitation $\langle b^\dagger b \rangle \ll N$, only the first few terms should be taken into consideration. For zero-th- and first-order approximations, we will separately discuss the linear and nonlinear regimes in the following sections.

S4. Scattering matrix in the linear regime

For a low excitation $\frac{\langle b^\dagger b \rangle}{N} \ll 1$, and applying the linear approximation $\sqrt{1 - \frac{b^\dagger b}{N}} \approx 1$ [Eq. (S9)], the Hamiltonian can be simplified to the form of two linearly coupled bosonic modes

$$H_l = \Delta a^\dagger a + \Delta' b^\dagger b + g_{\text{eff}} (a^\dagger b + ab^\dagger). \quad (\text{S10})$$

Due to the collectively enhanced effective coupling strength $g_{\text{eff}} = g\sqrt{N}$, the cavity mode and the collective atom spin are hybridized and constitute the atom-cavity polariton states p_u and p_l . They are linear combinations of mode a, b and can be derived by solving the eigenvector of the matrix

$$\mathbf{H} = \begin{pmatrix} \Delta & g_{\text{eff}} \\ g_{\text{eff}} & \Delta' \end{pmatrix}. \quad (\text{S11})$$

The Hamiltonian can be diagonalized to $H = \Delta_u p_u^\dagger p_u + \Delta_l p_l^\dagger p_l$, with the eigenfrequencies of the cavity polaritons being

$$\Delta_{u,l} = \Delta + \frac{\Delta_{ac} \pm \sqrt{\Delta_{ac}^2 + 4g_{\text{eff}}^2}}{2}. \quad (\text{S12})$$

For $g_{\text{eff}} > \kappa, \gamma$, typical anti-crossing spectra should be observed.

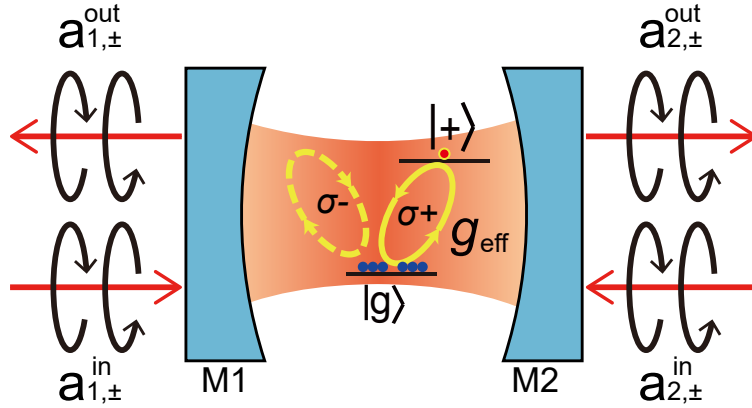


FIG. S4. Input and output modes at two different F-P cavity mirrors. The subscript 1 (2) denotes the mode at the left (right) mirror, and + (−) denotes the right-handed (left-handed) polarization.

In our experiment, there are σ_+ - and σ_- -polarized modes (b_{\pm}) coupling with atoms. Due to the population of atoms on hyperfine ground states, we have the effective coupling strength between atoms to the two modes are orthogonal and different. Therefore, we introduce effective coupling strengths $g_{\text{eff},\pm}$ for the coupling strength weighted by the Clebsch-Gordan coefficients and population distributions. For a probe field with strength of ε_p , i.e.,

$$H_p = \sqrt{2\kappa_1} \varepsilon_p (a + a^\dagger), \quad (\text{S13})$$

the dynamics of the system follows

$$\frac{d}{dt} a = (-i\Delta - \kappa) a - ig_{\text{eff},\pm} b_{\pm} + \sqrt{2\kappa_1} \varepsilon_p, \quad (\text{S14})$$

$$\frac{d}{dt} b_{\pm} = (-i\Delta' - \gamma) b_{\pm} - ig_{\text{eff},\pm} a, \quad (\text{S15})$$

where κ is the cavity decay rate, $\kappa_{1,2}$ is the coupling strength to the cavity modes through mirrors 1 and 2, and γ is the atom decay rate. The steady-state cavity field is obtained at $\frac{d}{dt} a = \frac{d}{dt} b_{\pm} = 0$. By the input-output formalism, the transmittance is derived as

$$T_{\pm} = \frac{4\kappa_1 \kappa_2}{\kappa^2} \left| \frac{1}{i\Delta/\kappa + 1 + 2C_{\pm}/(i(\Delta + \Delta_{ac})/\gamma + 1)} \right|^2, \quad (\text{S16})$$

where $C_{\pm} = g_{\text{eff},\pm}^2/2\kappa\gamma$ is the cooperativity. For all atoms prepared to the Zeeman sublevel, coupling with σ_- light is forbidden, i.e., $C_- = 0$, the maximum isolation ratio

$$\mathcal{I}_0 = (1 + 2C_+)^2 \quad (\text{S17})$$

could be achieved for $\Delta = \Delta_{ac} = 0$.

To fully characterize the nonreciprocal property of the system, we can investigate the scattering matrix that links the input and output ports. Considering the two input/output modes at two different cavity mirrors and two polarization states of each mode (as shown in Figure S4), the input-output relationship is described by

$$\begin{pmatrix} a_{1,+}^{\text{out}} \\ a_{1,-}^{\text{out}} \\ a_{2,+}^{\text{out}} \\ a_{2,-}^{\text{out}} \end{pmatrix} = \mathbf{S} \cdot \begin{pmatrix} a_{1,+}^{\text{in}} \\ a_{1,-}^{\text{in}} \\ a_{2,+}^{\text{in}} \\ a_{2,-}^{\text{in}} \end{pmatrix}, \quad (\text{S18})$$

where the subscript 1 (2) denotes the mode at the left (right) mirror and + (−) denotes the right-handed (left-handed) polarization, and the scattering matrix is

$$\mathbf{S} = \begin{pmatrix} 0 & 1 - \sqrt{\frac{\kappa_1}{\kappa_2}} t_- & t_+ & 0 \\ 1 - \sqrt{\frac{\kappa_1}{\kappa_2}} t_+ & 0 & 0 & t_- \\ t_+ & 0 & 0 & 1 - \sqrt{\frac{\kappa_2}{\kappa_1}} t_- \\ 0 & t_- & 1 - \sqrt{\frac{\kappa_2}{\kappa_1}} t_+ & 0 \end{pmatrix}, \quad (\text{S19})$$

where

$$t_{\pm} = \frac{2\sqrt{\kappa_1 \kappa_2}}{\kappa} \frac{1}{i\Delta/\kappa + 1 + 2C_{\pm}/(i(\Delta + \Delta_{ac})/\gamma + 1)}. \quad (\text{S20})$$

The scattering matrix for intensity is

$$\mathbf{S}_{\mathbf{I}} = \begin{pmatrix} 0 & \left(1 - \sqrt{\frac{\kappa_1}{\kappa_2}} T_-\right)^2 & T_+ & 0 \\ \left(1 - \sqrt{\frac{\kappa_1}{\kappa_2}} T_+\right)^2 & 0 & 0 & T_- \\ T_+ & 0 & 0 & \left(1 - \sqrt{\frac{\kappa_1}{\kappa_2}} T_-\right)^2 \\ 0 & T_- & \left(1 - \sqrt{\frac{\kappa_1}{\kappa_2}} T_+\right)^2 & 0 \end{pmatrix} \quad (\text{S21})$$

with T_{\pm} the same as that in Eq. S16. For a reciprocal system, the scattering matrix fulfills $\mathbf{S} = \mathbf{S}^T$ ($\mathbf{S}_{\mathbf{I}} = \mathbf{S}_{\mathbf{I}}^T$). For our system, since $C_+ \neq C_-$, it can be directly inferred that $\mathbf{S} \neq \mathbf{S}^T$ ($\mathbf{S}_{\mathbf{I}} \neq \mathbf{S}_{\mathbf{I}}^T$) and the reciprocity is broken by the different atom-cavity coupling strengths. At the experimental condition with $C_+ \gg 1$, $C_- = 0$ and $\Delta = \Delta_{ac} = 0$, $T_+ \approx 0$ and $T_- = \frac{4\kappa_1 \kappa_2}{\kappa^2}$, the matrix can be simplified as

$$\mathbf{S}_{\mathbf{I}} = \begin{pmatrix} 0 & \left(1 - \frac{\kappa_1}{\kappa}\right)^2 & 0 & 0 \\ 1 & 0 & 0 & T_- \\ 0 & 0 & 0 & \left(1 - \frac{\kappa_2}{\kappa}\right)^2 \\ 0 & T_- & 1 & 0 \end{pmatrix}, \quad (\text{S22})$$

and thus breaks Lorentz reciprocity.

If we only consider transmitting paths shown as a1 to b1 and a2 to b2 in Figure 2a in the main text and omit the reflections of the PBSs, the whole device can be seen as a black box. Both the input and output are horizontally polarized; thus, the scattering matrix is a two-port matrix. The scattering matrix can be expressed as $\mathbf{S}_{\mathbf{I}} = \begin{pmatrix} 0 & T_+ \\ T_- & 0 \end{pmatrix}$ and we have $\begin{pmatrix} b_1 \\ b_2 \end{pmatrix} = \mathbf{S}_{\mathbf{I}} \begin{pmatrix} a_1 \\ a_2 \end{pmatrix}$. Under the experimental conditions mentioned above, the scattering matrix is then $\begin{pmatrix} 0 & 0 \\ \frac{4\kappa_1 \kappa_2}{\kappa^2} & 0 \end{pmatrix}$ and the Lorentz reciprocity is broken.

S5. Individual cavity polaritons under coherent driving

For the first-order approximation of the Taylor series [Eq. (S9)], the nonlinear term

$$H_{nl} = -\frac{g_{\text{eff}}}{2N} (a^\dagger b^\dagger b b + a b^\dagger b^\dagger b) \quad (\text{S23})$$

should be considered, which involves the four-excitation interaction between modes a and b . In the picture of polaritons, the Hamiltonian is written as

$$H = \Delta_u p_u^\dagger p_u + \Delta_l p_l^\dagger p_l + \sum_{ijkm} \eta_{ijkm} p_i^\dagger p_j^\dagger p_k p_m + h.c.,$$

where $i, j, k, m \in \{u, l\}$ and η_{ijkm} is the nonlinear interaction strength, $p_{u,l} = \frac{(a \pm b)}{\sqrt{2}}$. For simplicity, we consider the case in which the cavity and atom are both resonant with the driving field $\Delta = \Delta' = 0$, and the Hamiltonian reduces to

$$H_{\text{eff}} = g_{\text{eff}} p_u^\dagger p_u - g_{\text{eff}} p_l^\dagger p_l - \frac{g_{\text{eff}}}{2N} \left[p_u^\dagger p_u^\dagger p_u p_u - p_l^\dagger p_l^\dagger p_l p_l - (p_u^\dagger p_u - p_l^\dagger p_l) (p_u^\dagger p_l + p_u p_l^\dagger) + (p_u^\dagger p_l - p_u p_l^\dagger) \right]. \quad (\text{S24})$$

The polaritons $p_{u,l}$ have resonant frequencies of $\Delta_{u,l}$ and experience Kerr nonlinearity with an effective coupling strength of $\mp \frac{g_{\text{eff}}}{2N}$, which are shown by the first two terms in the second line. The third and last terms in the second line describe the mode conversion between the two polariton states. For a large atom number N , a similar treatment can also be extended to situation where the atoms are not uniformly coupled to the cavity since the correlation between atoms can be neglected.

First, we investigate the properties of individual cavity polariton states under coherent driving. The interaction Hamiltonians are the self-Kerr (self-phase modulation) terms $H_I = -\frac{g_{\text{eff}}}{2N} p_u^\dagger p_u^\dagger p_u p_u$ and $H_I = +\frac{g_{\text{eff}}}{2N} p_l^\dagger p_l^\dagger p_l p_l$. Since N is very large, the nonlinearity of both polariton states is too weak to induce a significant single photon nonlinear effect, such as the polariton blockade effect, in neither p_u nor p_l . Figure S5 shows the frequency dependence of the intracavity excitation number and the second-order correlation of each polariton state. The two curves represent $g_{\text{eff}} = \pm 8.4947 \kappa$, corresponding to the case of the $p_{l,u}$ mode. Since the Kerr nonlinearities of different signs shift the polariton resonance in opposite directions, both curves shift slightly away from zero detuning. Additionally, the polariton state exhibits anharmonicity, and the energy level of the Fock state $|n\rangle$ shifts by $\frac{g_{\text{eff}}}{2N} n(n-1)$, which is demonstrated by the second-order correlation function $g^{(2)}(0)$ of the field. For the case of p_u with negative Kerr nonlinearity $-\frac{g_{\text{eff}}}{2N}$, the transition frequency between adjacent Fock states $|n\rangle$ and $|n+1\rangle$ is detuned by $-\frac{g_{\text{eff}}}{2N} 2n$. Therefore, the photon blockade effect is expected when probed on the blue side, and sub-Poisson distribution is observed. For the probe on the red side, a Fock state higher than $|1\rangle$ can be more efficiently excited than the coherent state; thus, the field shows super-Poisson statistics. A similar analysis can be applied to the p_l polariton, which indicates an opposite result.

Note that the self-Kerr nonlinearity scales inversely with the atom number N . As the number of atoms increases to a sufficiently large value, the impact of the nonlinearity will become weak so that the resonance shift and the nonclassical statistics are negligible. In our calculation, $g_{\text{eff}} = 8.4947$ and $N = 55$, and only a 5% deviation of $g^{(2)}(0)$ from 1 is observed.

S6. Quantum interference between cavity polaritons

In the strongly coupled cavity-atom system, the hybridization of the cavity mode and bosonic collective spin mode constitute two cavity polaritons. They can be excited selectively or simultaneously by choosing an appropriate frequency of the probe field. Under coherent field probing on the cavity mode, these two polaritons are simultaneously probed with coherent fields (Eq. (S13)), described by the Hamiltonian

$$H_p = \varepsilon_{p_u} (p_u^\dagger + p_u) + \varepsilon_l (p_l^\dagger + p_l), \quad (\text{S25})$$

with $\varepsilon_{p_{u,l}}$ being the effective driving strength. In addition to the self-Kerr nonlinearity of individual polaritons, they also exchange energy with each other (Eq. S24). Therefore, each polariton is excited in two ways: coherent driving and coherent conversion from the other polariton. Here, the response of the polariton under coherent driving is investigated with the experimental parameters $g_{\text{eff}} = 8.4947$ for σ_- light and $g_{\text{eff}} = 4.6424$ for σ_+ light, with the atom number set to $N = 55$.

Since the probe field to the cavity can excite two polariton states simultaneously, an interesting quantum effect arises due to the interference between the optical emissions of $p_{u,l}$. As shown in Figure S6, the frequency dependence of the polariton excitation and $g^{(2)}(0)$ are investigated numerically. Since the frequencies of the polariton states are different, when the probe is near

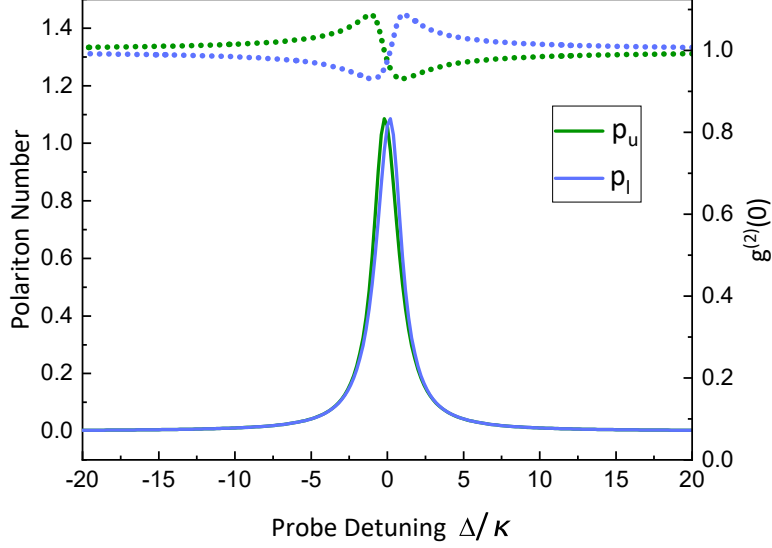


FIG. S5. Basic properties of a single cavity polariton with self-Kerr nonlinearity. (Solid lines) Relationship between the mean excitation number and the driving frequency. (Dotted lines) Relationship between the second-order correlation $g^{(2)}(0)$ and the driving frequency. The calculations are performed with the following parameters: number of atoms $N = 55$, atom-cavity coupling strength $g_{\text{eff}} = 8.4947$, driving strength $\varepsilon_p = \sqrt{1.1}$, cavity decay rate $\kappa = 1$, and atom decay rate $\gamma = 0.71233$.

resonant with one polariton state, the influence of the other polariton state is negligible. As shown in Figure S6 (middle and right panels), the spectrum shows similar behaviors to Figure 1 in the main text when the probe is near resonant with p_u or p_l . In particular, $g^{(2)}(0)$ shows a small modification due to the self-Kerr effect of polaritons. It should also be noted that when the probe field is tuned to resonate with the other polariton, for example, p_l in the left panel of Figure S6, a significant $g^{(2)}(0)$ pattern is also observed for the p_u polariton even though it is not efficiently excited. More interestingly, the $g^{(2)}(0)$ pattern of p_u is more pronounced than that of the resonant excitation. Such an unusual phenomenon could be accounted for by the interference between the directly excited p_u and the conversion from p_l since p_l is efficiently excited. These two processes both possess Kerr nonlinearity and alter the phase of Fock states higher than $|1\rangle$ in different manners, thus suppressing or enhancing the components of high-order Fock states according to the driving frequency, leading to bunching or anti-bunching of the polariton field.

In experiments, the quantum statistics can only be measured for the cavity output field, which is a combination of both polariton states. The middle panel of Figure S6 shows the equivalent cavity photon number and $g^{(2)}(0)$ against the probe frequency. The two peaks of each curve clearly show the resonances of polariton states. As an example, we explain the σ_- case in which the cavity and atoms share the same frequency. As shown by the blue curve in Figure S5, the curve can be divided into three regions. On the left, the probe field is near-resonance with p_l and far off-resonance with p_u . The cavity field is mainly contributed by p_l ; thus, its second-order correlation behaves the same with p_l (shown by the right panel of Figure S6). Similarly, the curve on the right side is the same as p_u in the left panel of Figure S6. For the case of a driving frequency near the center of the polariton frequencies (the middle of the middle panel of Figure S6), p_u and p_l are simultaneously excited with approximately equal strength, and the output cavity field is now a superposition of the emission from two polariton states. In this case, significant interference is expected. Due to the opposite sign of $p_u^\dagger p_u^\dagger p_u p_u$ and $p_l^\dagger p_l^\dagger p_l p_l$, the most significant term in the Fock space, i.e., the two-photon state $|2\rangle$ have opposite phases. Therefore, the component of $|2\rangle$ is strongly suppressed after the projection of the polaritons to the cavity field if the polaritons are symmetrically excited. This phenomenon is similar to the unconventional photon blockade [60], by which significant anti-bunching can be observed with only very weak nonlinearity. The most significant destructive interference is expected when excitations of two polariton states are the same. In our calculation, a nearly zero $g^{(2)}(0)$ is observed with nonlinearity as low as $g_{\text{eff}}/N = 0.077 \kappa$, as shown by the dotted blue curve. If the probe field is shifted slightly away from the maximum point, the nonlinear phases induced by two polaritons change, leading to constructive interference and bunching of the cavity field with $g^{(2)}(0) > 1$. By exploiting the interference between cavity polaritons, the analysis clearly reveals the mechanics of quantum statistics in cavity QED system containing many emitters without numerically calculating the system in an exponentially scaled Hilbert space.

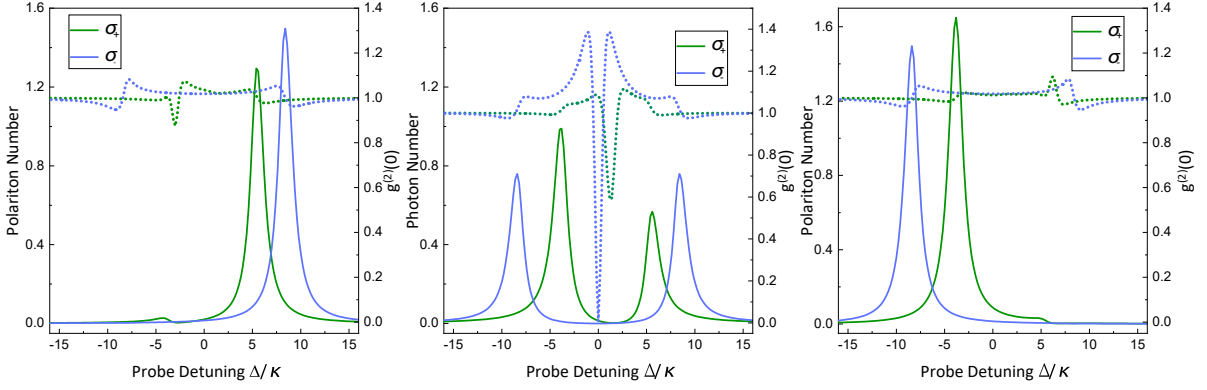


FIG. S6. Mean excitation number and second-order quantum correlation $g^{(2)}(0)$ of the cavity mode and cavity-atom modes. Left: polariton state p_u ; Middle: cavity field; Right: polariton state p_l . The parameters are $\kappa = 1$, $\gamma = 0.7123$, $\epsilon_p = \sqrt{2.2}$, and $N = 55$. For the σ_+ case, $g_{\text{eff}} = 4.4624$ and the cavity-atom detuning $\Delta_{ac} = 4.6438$. For the σ_- case, $g_{\text{eff}} = 8.4947$ and the atom is in resonance with the cavity. Solid line: mean excitation number (left axis). Dashed line: second-order correlation function $g^{(2)}(0)$ (right axis)

S7. Nonreciprocity of the cavity polaritons

In the following, we compare the two cases where the atoms are initially prepared in different Zeeman sublevels and probed by light with different circular polarizations, and show the nonreciprocity of the cavity-polaritons. As presented in the main text, the coupling strength g for the σ_{\pm} -polarized cavity mode is different when the atoms are prepared to a Zeeman state that breaks the time-reversal symmetry. According to the experimental parameters, the numerical results in Figure S6 show non-reciprocal mean-field and second-order correlation functions, as the spectra are different for the $(+z, \sigma_+)$ and $(-z, \sigma_-)$ probes.

By probing the system from different directions with different polarizations, the non-reciprocal excitation of the polaritons is expected, as can be measured by the non-reciprocal transmission of the cavity field. Such non-reciprocal phenomena mainly result from the difference in the atom-photon coupling strength or the cooperativity of the system. Additionally, compared with the σ_- case, the transition between atom energy levels that couples with the σ_+ light is shifted away from the cavity resonance due to the Stark shift Δ_{Stark} , which agrees well with the experimental results. Therefore, the resonances of the polaritons are asymmetric for σ_+ coupling.

In addition, the quantum statistics of the polaritons are also non-reciprocal. Since they have different resonant frequencies, nonclassical statistics appear only when they are nearly resonant-excited, while they almost behave classically for far-off resonant excitation. Such non-reciprocal quantum statistics of polaritons are shown by the blue (σ_-) and green (σ_+) dashed curves. For example, if the system is probed by light with frequency detuning $\Delta/\kappa = 7$, the polariton p_u of σ_- coupling shows sub-Poisson statistics, while the σ_+ coupling shows super-Poisson statistics (left panel of Figure S6). The non-reciprocal quantum statistics of polaritons are the most significant when the probe is near the resonances.

S8. Non-reciprocal quantum interference

In the last section, we focused on the quantum interference between cavity polaritons, which is reflected by the second-order correlation $g^{(2)}(0)$ of the cavity field. It was noted that the quantum interference of two paths requires them to have nearly the same amplitude. In our system, the most significant parameter that influences the excitation of two cavity polaritons is the relative detuning of the probe field. When probed with frequency near the center of the two polaritons, strong quantum interference is observed, indicated by the significant interference pattern of the $g^{(2)}(0)$ of the cavity field (dashed curve, Figure S6). Due to the AC-Stark shift, the resonances of the σ_- polaritons are symmetrically spaced on different sites of the cavity resonance, while the resonances of the σ_+ polaritons are asymmetric with p_l near the cavity resonance and p_u far from it. Therefore, the strongest quantum interference occurs at $\Delta = 0$ for σ_- , where the two polaritons are balanced excited. For σ_+ , the probe frequency should be shifted toward p_u to balance the excitations. At the balanced point, the destructive interference greatly suppresses the population of large photon-number states, leading to anti-bunching of the cavity output field. With a small detuning, the constructive interference results in bunching of the cavity field.

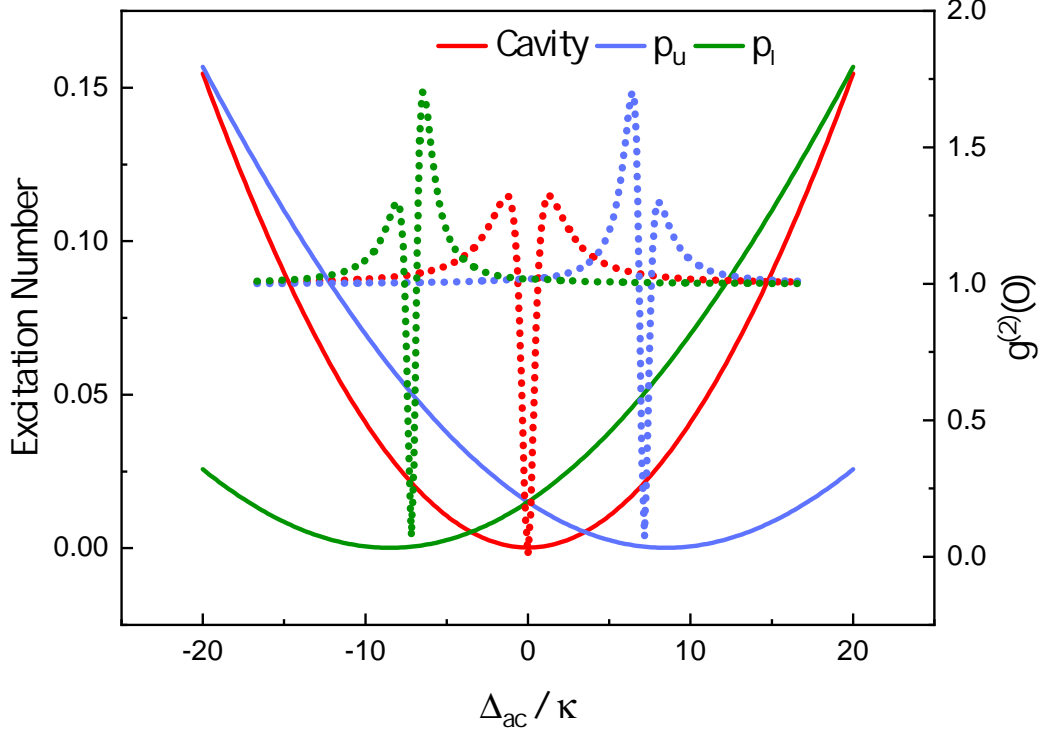


FIG. S7. The mean excitation number and the second-order correlation function $g^{(2)}(0)$ of the polaritons versus the cavity-atom detuning Δ_{ac} . The parameters are $\kappa = 1$, $\gamma = 0.7123$, $\varepsilon_p = \sqrt{2.2}$, $N = 55$, and $g_{\text{eff}} = 8.4947$.

The nonreciprocity of the quantum interference depends on the cavity-atom detuning Δ_{ac} , which is shown in Figure S7. Under resonant probe $\Delta = 0$, p_u is efficiently excited for negative detunings and suppressed for positive detunings (blue curve, Figure S7), vice versa for p_l . Its second-order correlation function $g^{(2)}(0)$ shows a significant interference pattern at an appropriate $\Delta_{ac} > 0$, at which p_u is suppressed and p_l is excited. Due to the coherent conversion from p_l to p_u , these two components are balanced at a critical value of Δ_{ac} and interfere with each other, leading to strong bunching and anti-bunching of the polariton. The solid and dashed red curves show the mean photon number and $g^{(2)}(0)$ of the cavity field, respectively, which also shows strong quantum interference.

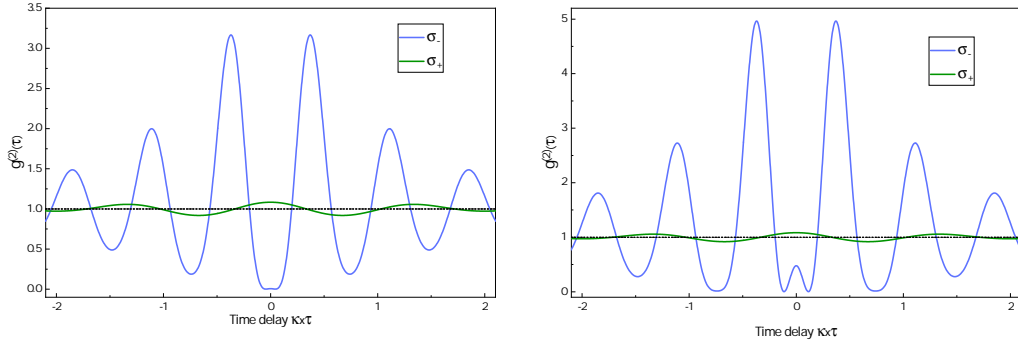


FIG. S8. Second-order correlation function $g^{(2)}(\tau)$ of the cavity field for σ_+ and σ_- driving. Left: $N = 55$. Right: $N = 35$.

In our experiment, the nonreciprocity of the quantum interference is tested at $\Delta = 0$. For resonant probe $\Delta = 0$, strong interference is indicated by $g^{(2)}(0)$, with $g^{(2)}(0) > 1$ for σ_+ and $g^{(2)}(0) < 1$ for σ_- (Figure S8). In this case, $g^{(2)}(\tau)$ oscillates with the time

delay τ , due to the beating between the polariton state. The oscillation period is proportional to the frequency difference of the two polariton states.

S9. Discussion

To summarize, the non-reciprocal transmission mainly depends on the cooperativity of the system for the σ_{\pm} mode that can only be separately probed from different directions, while the non-reciprocal quantum statistics are very sensitive to the atom-cavity detuning due to quantum interference between polariton states. Compared with single-emitter cavity QED, the multiatom system can achieve larger cooperativity via the collective effect, which is beneficial for applications, such as high-isolation ratio non-reciprocal devices with higher saturation power. For the study of fundamental physics, the quantum property of cavity polaritons behaves differently, which depends on the atom number N , coupling strength g and driving field ε_p . A high cooperativity system can be constructed either by a few atoms coupled to a cavity with strong interaction strength or many atoms with weak interaction strength. These two systems have distinct quantum statistics, as seen in Figure S9. The blue line in Figure S9 shows the second-order correlation function of the cavity field in systems with fixed g_{eff} . As the number of atoms increases, the statistics of the cavity field change from super-Poisson to sub-Poisson. For a very large atom number N , the $g^{(2)}(0)$ of the cavity field increases and approaches 1 due to the decrease in the nonlinearity $\frac{g_{\text{eff}}}{2N}$ of a single cavity polariton. Our experimental study lies in the moderate region where the cavity polaritons are not saturated and their nonlinearity is relatively large. It should be noted that the treatment that includes only the first two orders of Eq. (S9) should be extended to higher-order series under strong excitation, offering a new platform to study high-order nonlinear effects.

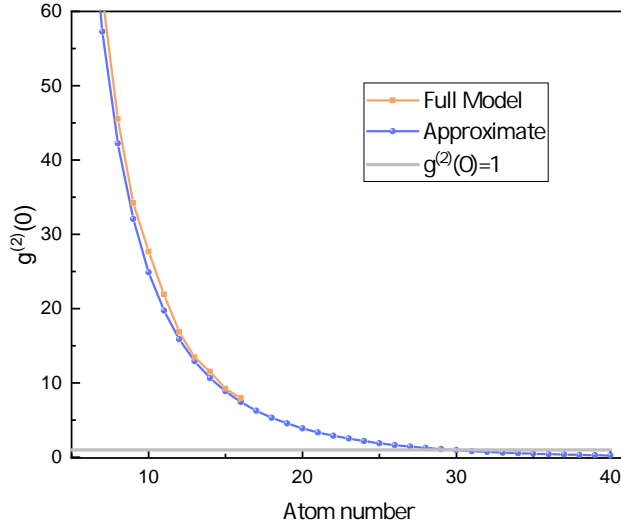


FIG. S9. Comparison between the numerical results of the full model and the approximate model. In the calculations, the cooperativity C is kept the same by increasing the atom number N and reducing the coupling strength g . The parameters used are $g\sqrt{N} = 8.4316$, $\kappa = 1$, $\gamma = 0.7123$, $\varepsilon_p = \sqrt{2.2}$, and $\Delta = \Delta_{ac} = 0$. Blue line: results by the model in Eq. (S24). Orange line: results by the model in Eq. (S1). As the atom number N increases, the results of the approximate mode based on the bosonic treatment of the collective atomic spin approach the results of the full Hamiltonian.

S10. Comparison with full-numerically result

In the above analysis, the system with effective total atomic spin $N/2$ is approximately treated as a bosonic mode. At the low-excitation limit, atomic nonlinearity in the few-atom ensemble is approximated to the first order of $1/N$. To verify the validity of the low-excitation approximation, we compare the results of the above model and the numerical solution of the full Hamiltonian [Eq. (S1)]. Because the dimension of the Hilbert space of the system exponentially increases with the number of atoms (N) as $d = M \times 2^N$, where M is the truncated dimension of the cavity mode, the computation complexity increases rapidly with increased pump power and number of atoms, and the numerical simulation is limited to a small N . Here, we use the quantum

trajectory approach to simulate the system evolution [61], which is less demanding for computation resources since only the pure state (dimension d) is considered in the quantum trajectory simulation instead of the density matrix (dimension d^2). We fix the value of $g_{\text{eff}} = g\sqrt{N}$, thus fixing the cooperativity C , and change the atom number N . In Figure S8, we plot the second-order correlation function $g^{(2)}(0)$ of the cavity output calculated from both the approximate and full models. The difference between the two curves decreases as the number of atoms increases, which verifies the validity of our analysis based on the approximate model.

S11. Simulation of reconfiguration of optical isolator

In our experiment, the switch of the isolation direction is realized by controlling the populations of the internal state of the atoms. As shown in Figure S10, the probe field (green arrows) is resonant to the $|6S_{1/2}, F=4\rangle \leftrightarrow |6P_{3/2}, F=3\rangle$ transition. The populations of the internal state of the atom are controlled by the 459-nm pump laser (blue arrows), which is resonant to the transition $|6S_{1/2}, F=4\rangle \leftrightarrow |7P_{1/2}, F=4\rangle$. The probe field with σ_- polarization transmits through the cavity when the atom is populated at $m_F = -4$ or -3 , while it is blockaded when the atom is populated in $m_F = 4$ due to vacuum Rabi splitting. It should be noted that the switch between transmission and blockade is asymmetric depending on the initial state of the atom. In our experiment, we use an ensemble of atoms that strongly couple to the atomic transition. For the transmission case, all the atoms are required to be in the $m_F = -4$ and $m_F = -3$ states. However, to block the probe field, only a small portion of atoms on $m_F \geq -2$ can induce significant Rabi splitting. If we start with the transmission case where all atoms are prepared at $m_F = -4$, the internal state of the atoms will be gradually pumped to $m_F \geq -2$ under a σ_+ pump field. The transmission of the probe will be switched off quickly as long as the states of several atoms are transferred. The larger the atom number and the stronger the vacuum coupling strength, the faster the switch-off speed. In contrast, when we start from the blockade state with all atoms prepared at $m_F = 4$, transferring all the atoms to $m_F = -3$ and $m_F = -4$ with a σ_- pump laser will take a sufficiently long time. The smaller the atom number and the weaker the vacuum coupling strength, the slower the switch-on speed.

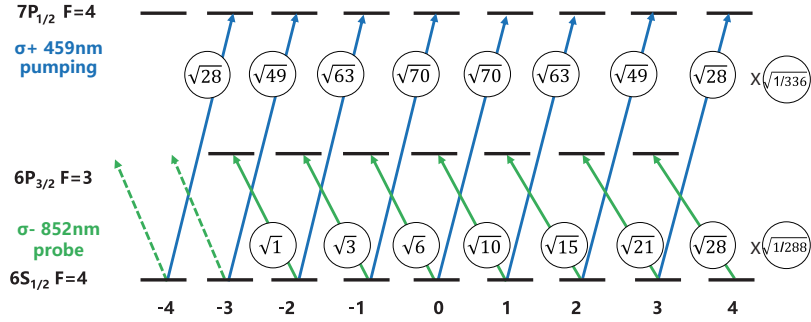


FIG. S10. Energy levels and optical pumping procedure. Atoms initially populated at $|6S_{1/2}, F=4, m_F=-4\rangle$. The probe field resonates to transition between $|6S_{1/2}, F=4\rangle$ and $|6P_{3/2}, F=3\rangle$, and the internal state of the atom is controlled by the 459-nm pump laser which couples to the transition between $|6S_{1/2}, F=4\rangle$ and $|7P_{1/2}, F=4\rangle$. The numbers inside the circles are the corresponding reduced dipole matrix elements.

To quantitatively study the switching process, we theoretically simulated the optical pumping process by taking all the experimental parameters. After switching the polarization of the 459-nm pump light, the variance of the atomic population on each Zeeman state can be obtained by using the rate equations, and the results are shown in Figure S11. A maximum Rabi frequency of 2.3Γ for the 459-nm optical light is used, and Γ is the decay rate of $|7P_{1/2}, F=4\rangle$. In this simulation, we only consider the effect of the pump laser and neglect that of the probe light since it is sufficiently weak. The variance of the effective parameter of cooperativity versus time is then obtained by

$$C_{\pm}^{\text{eff}} = N \sum_i \rho_{ii} g_{i,\pm}^2 / 2\kappa\gamma, \quad (\text{S26})$$

where ρ_{ii} is the population of $m_F = i$, N is the total atom number, and $g_{i,\pm}$ is the coupling strength between $m_F = i$ and $m_{F'} = i \pm 1$. The dependence of C_{\pm}^{eff} on time is shown in Figure S12a. The transmittance of the probe field can be calculated by using Eq. (1) in the main text, and the results are given in Figure S12b. The theoretical results are in good agreement with the experimental results.

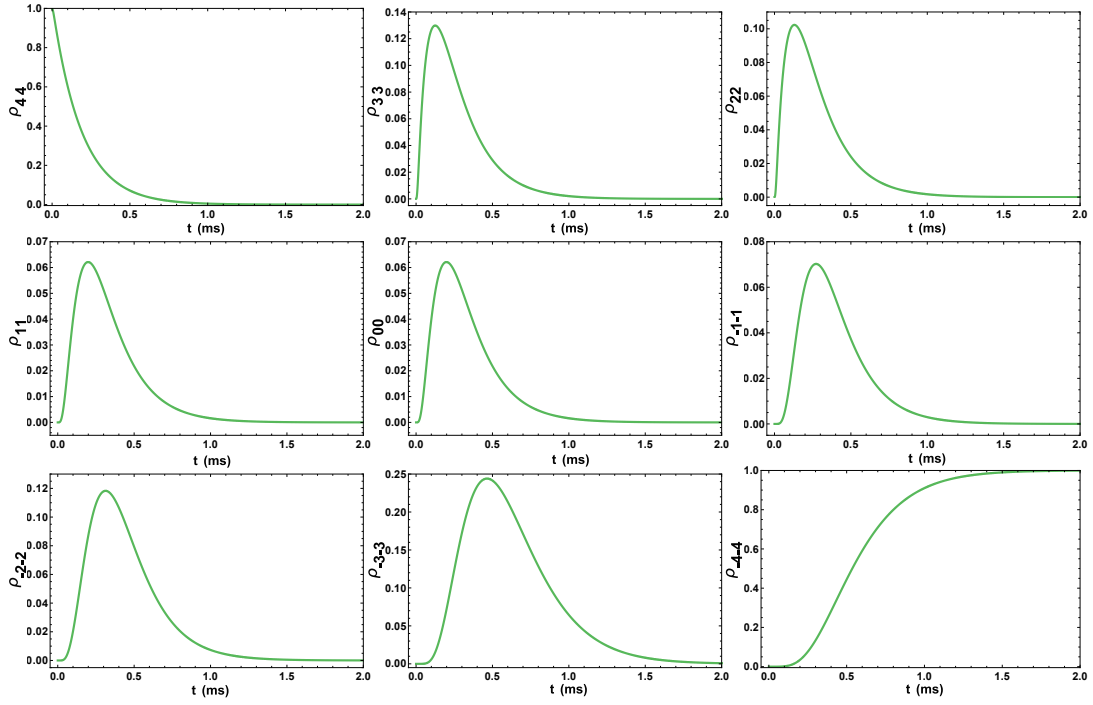


FIG. S11. Atomic population (ρ_{ii}) versus time during the turn-on procedure. A σ_- 459-nm pump laser is used to continuously pump the atoms from $m_F = 4$ to $m_F = -4$ with an optical pumping rate equal to 2.3Γ . The 459-nm pumping light with polarization σ_+ is turned on at $t = 0$.

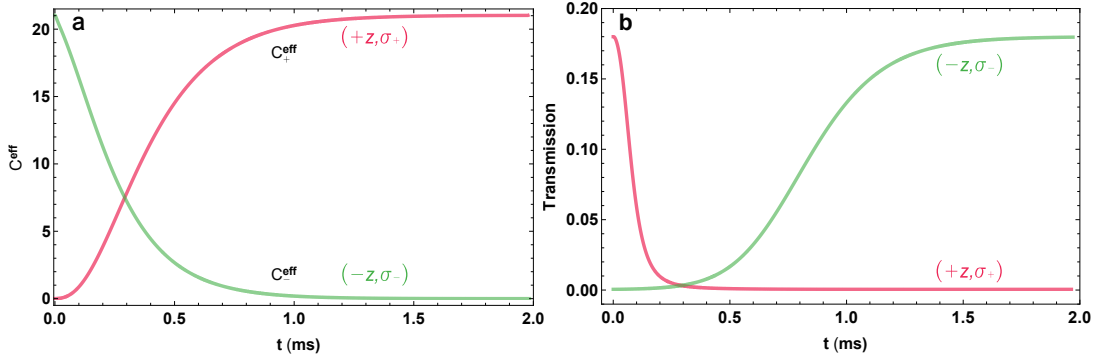


FIG. S12. The effective cooperativity and transmission versus time during the switch procedure. A 459-nm pump laser is used to continuously pump the atoms between $m_F = -4$ and $m_F = 4$ with the same optical pumping rate in Figure 4. (a) The variance of effective cooperativity as the shut-off (red curve) and turn-on (green curve) procedures. (b) The corresponding transmission during the same procedures as in (a). The 459-nm pumping light with polarization σ_+ is turned on at $t = 0$.